Tumor suppressive activities of the cohesin SA1/STAG2 and effects of PARP impairment during *Drosophila* brain development

Simona Totaro[1,2], Antonella Lettieri[2], Silvia Castiglioni[2], Francesco Lavezzari[1], Cristina Gervasini[2], Valentina Massa[2,*], and Thomas Vaccari[1,*]

[1]Department of Biosciences, Università degli Studi di Milano, Milan, Italy

[2]Department of Health Sciences, Università degli Studi di Milano, Milan, Italy

[*]Authors for correspondence: valentina.massa@unimi.it thomas.vaccari@unimi.it

ABSTRACT

The cohesin complex performs essential cellular functions including regulation of chromatin organization and DNA repair. Somatic pathogenetic variants in cohesin genes, such as *STAG2*, have been associated with cancer, but their contribution to brain tumorigenesis is unclear. Here, we report the presence of *STAG2* variants in glioblastoma and medulloblastoma patients and determine the effects of loss of *STAG2* in human cells and of the homolog *SA1* in *Drosophila* tissues. Reduction of *SA1* expression during fly brain development leads to defects in neural stem cells differentiation and promotion of tumorigenesis, both in the presence of oncogenic activity and *per se*. Treatment with inhibitors of the Poly ADP-ribose polymerase (PARP), which are used to treat forms of cancer with defects in DNA repair, in combination with *STAG2/SA1* depletion resulted in apoptosis *in vitro* and *in vivo*. In flies, reduction of PARP activity ameliorated the tumor associated phenotypes of *SA1*-deficient tissue. Our *in vivo* and *in vitro* data suggest that impairment of PARP activity compensates for reduced cohesin activity, highlighting a vulnerability that might be pharmacologically exploited in brain tumors.

Keywords: Drosophila, STAG2, cohesin complex, PARP inhibitor

INTRODUCTION

Cohesin proteins are part of a conserved ring complex that ensures sister chromatid cohesion (Nasmyth, 2011). The cohesin complex also regulates genomic stability by taking part in DNA repair (Nasmyth and Haering, 2009). In addition, it orchestrates gene expression by acting on the genome 3D architecture and therefore, by participating in chromatin remodeling (Nasmyth and Haering, 2009). While cohesin genes are essential for survival, heterozygous germline loss of

function variants cause congenital disorders called cohesinopathies, including Cornelia de Lange and Roberts syndromes (Kline *et al.*, 2018).

In humans, the cohesin core complex is formed by SMC1A, SMC3, RAD21 and STAG1, STAG2 or STAG3 (Nasmyth and Haering, 2009). While STAG3 is essential for proper chromosome pairing and segregation in meiosis (Bayés *et al.*, 2001), STAG1 and STAG2 have broader, partially overlapping functions. However, STAG2 is specifically required for transcriptional regulation of DNA repair (Romero-Pérez *et al.*, 2019).

Owing to the many tumor suppressive processes in which the cohesin complex is involved, somatic pathogenic variants in multiple cohesin genes were found in several types of tumors (Di Nardo, Pallotta and Musio, 2022). In particular, *STAG2* is a frequent target of inactivating mutations in human cancers (Hill, Kim and Waldman, 2016; Arruda *et al.*, 2020). These usually include frameshift, nonsense, or splice site mutations leading to aberrant proteins (De Koninck and Losada, 2016). *STAG2* variants were identified in a variety of tumors, including glioblastoma, (Solomon *et al.*, 2011), urothelial bladder cancer (Balbás-Martínez *et al.*, 2013; Guo *et al.*, 2013; Solomon *et al.*, 2013; Taylor *et al.*, 2014; Tirode *et al.*, 2014; Weinstein *et al.*, 2014), melanoma (Solomon *et al.*, 2011) myelodysplastic syndrome, acute myeloid leukemia (Solomon *et al.*, 2011) and Ewing's sarcoma (Brohl *et al.*, 2014; Crompton *et al.*, 2014). Somatic variants in *STAG1* are also involved in the tumorigenesis of colorectal cancer, bladder cancer, Ewing's sarcoma and myeloid malignancies (Balbás-Martínez *et al.*, 2013; Kon *et al.*, 2013; Thota *et al.*, 2014; Weinstein *et al.*, 2014).

Cohesin genes are functionally conserved in *Drosophila melanogaster*. In particular, the fly genome encodes two homologs of human *STAG1-3*. *Stromalin1* (*SA1 or* CG3423) is ubiquitously expressed and appears to be related to *STAG1-2*, while *SA2* (CG13916) is mainly expressed in male gonads and is likely functionally similar to *STAG3* (Thomas *et al.*, 2005). *SA1* was initially identified with other fly cohesin genes for its ability to bind chromatin and regulate enhancer-promoter communication and support sister chromatid cohesion (Rollins *et al.*, 2004; Gause *et al.*, 2008). During embryogenesis, *SA1* expression is controlled by Notch target Cut in neuroblasts (NB) and supports developmentally regulated NB death, preventing the emergence of ectopic NBs. Such process appears to depend on cohesin ability to regulate chromatin architecture (Arya *et al.*, 2019). In the developing larval fly brain, *SA1* has also been implicated in post-mitotic regulation of morphogenesis, in particular in neuronal pruning, a process dependent on transcriptional regulation (Schuldiner *et al.*, 2008), as well as in establishing the pool of synaptic vesicles for memory formation (Phan *et al.*, 2019). In contrast to physiology, *SA1* contribution to tumor biology has not yet been assessed in flies. Despite this, a number of genetic manipulations in *Drosophila* have been previously used to assess the contribution of specific genes to brain tumorigenesis (Read *et al.*, 2009; Paglia *et al.*, 2017; Maurange, 2020).

The poly ADP-ribose polymerase (PARP) is a central sensor of DNA damage (D'Andrea, 2018). Drugs that inhibit PARP activity are currently used to induce synthetic lethality of breast and ovarian cancer cells with mutations in genes regulating DNA repair pathways (D'Andrea, 2018; Mekonnen, Yang and Shin, 2022). A few lines of evidence in *in vitro* systems have reported that depletion of *STAG2* causes susceptibility to PARP inhibitors (Bailey *et al.*, 2014; Liu *et al.*, 2018; Mondal *et al.*, 2019; Zhou *et al.*, 2023; Luo *et al.*, 2024). While the first evidence of *STAG2* involvement in tumorigenesis was the presence of focal deletions on the X chromosome in glioblastoma (Solomon *et al.*, 2011), no animal models of brain tumorigenesis based on reduced *STAG1/2* in somatic cells exist and no study of the effect of PARP inhibitors *in vivo* has been reported.

Here, we updated the repertoire of *STAG2* variants associated with glioblastoma and medulloblastoma. We have found that *STAG2* depletion in human spheroids leads to persistent DNA damage and that treatment with a PARP inhibitor increased the amount of apoptosis, when compared to untreated samples. To model the effect of somatic *STAG2* deficiency *in vivo*, we reduced the expression of *Drosophila* homolog *SA1* in multiple tissues during development. In larval wing disc, reduced expression of *SA1* and impairment of the activity of *Parp1*, the unique homolog of human PARP enzymes, lead to additive stabilization of DNA damage and to caspase activation. These phenotypes correlate with amelioration of the adult wing morphology, when compared to single manipulation. In a larval model of gliomagenesis, we find that reduced *SA1* expression causes excess tissue growth, which is prevented by the reduction of *Parp1* expression. Finally, in larval type II NBs (NBII), a type of neural stem cells that give rise to neurons and glia, upon *SA1* expression reduction we observed a delay of differentiation that is accompanied by occasional formation of masses in adult brains and shortened lifespan. *Parp1* depletion reverted *SA1* NBII phenotypes. Our data indicate that cohesin genes act as tumor suppressors and that their loss can be compensated by PARP inactivation *in vivo*. Thus, brain tumors with cohesin variants might represent potential therapeutic targets for PARP inhibitors.

RESULTS

STAG2 variants are present in glioblastoma and medulloblastoma patients

To evaluate the presence of *STAG2* variants in patients diagnosed with glioblastoma multiforme or medulloblastoma, we examined the publicly accessible cBioPortal, selecting datasets from 8 studies encompassing 1538 patients. We detected *STAG2* variants in 21 patients (2%), specifically, 5 missense, 7 nonsense, 6 splicing mutations, and 3 frameshifts. 8 were found in medulloblastoma and 13 in glioblastoma patients (colored dots in **Fig. 1A**). These changes were distributed

throughout the gene, involving the entire amino acid (aa) sequence of STAG2. Despite the lack of mutational hotspots, we observe that 4 out of the 8 medulloblastoma STAG2 variants occur within 39 aa corresponding to the end of the stromal antigen (STAG) domain and the beginning of the stromal in conserved domain (SCD) domain. For the medulloblastoma-associated variants, we also observe no association between a particular type of aa change with molecular subtypes (**Fig. 1A**).

When compared to variants associated with Mulleghama-Klein-Martinez syndrome, a rare X-linked neurodevelopmental disorder caused by mutations in the *STAG2* (Mullegama *et al.*, 2017), the glioblastoma multiforme or medulloblastoma variants were assigned a CADD score (see Methods for details) well above the average (**Fig. 1A**), suggesting that they might lead to reduced STAG2 function. Notably, in two patients with medulloblastoma (Group 3 and WNT group), the same variant, R259*, was reported. Patient details are listed in **suppl. Table 1**. The bioinformatic analysis suggests that somatic mutations in brain cancer might lead to partial or total loss of *STAG2* function.

Synergism of STAG2 knock-down and PARP inhibition in an *in vitro* model

To test the primary consequences of reduced *STAG2* function *in vitro*, we developed a cell model based on *STAG2* silencing in non-transformed cells. To this end, we stably integrated in HEK-293T cells a lentiviral plasmid expressing a short hairpin against *STAG2* (shSTAG2) or a scrambled sequence (SCR) as a control. To assess *STAG2* knockdown, we evaluated the expression of both *STAG2* mRNA and protein. We observed that STAG2 was significantly depleted in HEK-293T shSTAG2, when compared with HEK-293T shSCR and HEK-293T ctrl (**Fig S1A**), leading to reduction of the protein expression (**Fig S1B-C**). Depletion did not cause significant changes in cell viability but influenced cell adhesion to the substrate (**Fig S1D-F**), consistent with previously reported cellular phenotypes observed upon *STAG2* depletion (Mondal *et al.*, 2019).

Considering that the cohesin complex is involved in DNA repair, we next prepared 3D HEK-293T cultures and investigated spheroids for the presence of DNA damage. To this end, we analyzed γH2AX positivity, a well-known DNA damage marker, by Western blot analysis. We observed that HEK-293T shSTAG2 spheroids show higher amounts of γH2AX when compared with HEK-293T shSCR or control spheroids **(Fig 1B-D**).

Given the increased DNA damage in STAG2-depleted cells and the reported susceptibility of cells with aberrant DNA repair mechanisms to PARP inhibitors, we assessed the possible effects of PARP inhibition in our *in vitro* model. Thus, we treated HEK-293T shSTAG2 and shSCR with 3-AB, a potent PARP inhibitor (Sodhi, Singh and Jaggi, 2010). After 72 hours of treatment, to detect the presence of apoptotic cells we performed a TUNEL assay or immunofluorescence

staining for cleaved caspase 3 (cCas3), a marker of apoptosis. We found that HEK-293T shSTAG2 spheroids treated with 3-AB displayed significantly higher cCas3 positivity when compared with DMSO-only HEK-293T shSTAG2 spheroids or with 3-AB-treated HEK-293T shSCR spheroids (**Fig. 1E,** quantified in **F**). HEK-293T shSTAG2 cells treated with 3-AB also showed significantly higher TUNEL positivity compared with both HEK-293T shSTAG2 treated with vehicle or 3-AB-treated HEK-293T shSCR cells (**Fig. S1G,** quantified in **H**). Overall, our *in vitro* data suggest the presence of a pharmaco-genetic synthetic lethal interaction between the loss of STAG2 and PARP activity, that might depend on DNA damage.

Reduction of *SA1* activity in *Drosophila melanogaster* affects DNA repair *in vivo*

To validate our *in vitro* results, we studied the consequences of somatic depletion of *Drosophila SA1* and *Parp1 in vivo*. To deplete *SA1*, we expressed TRiP.GL00534 or TRiP.HMS00272, two hairpins to induce RNA interference (RNAi) against *SA1*. To reduce expression in cells of the dorsal side of larval wing imaginal discs, a monolayer epithelial tissue that gives rise to the adult wing, we used the driver *ms1096Bx-Gal4*. We co-expressed UAS-GFP to mark the tissue impacted by the downregulations (**Fig. 2A**). Compared to mock downregulation of luciferase (*MS>luc-RNAi*), TRiP.GL00534 (SA1-RNAi hereafter) resulted in slightly more efficient than TRiP.HMS00272 in downregulating *SA1* expression levels (**Fig. S2A**). Thus, we selected it for further analyses. *Parp1* depletion, achieved by expression of the GD9445 RNAi hairpin (*MS>Parp1-RNAi)*, caused nucleolar fragmentation, as previously reported (Boamah *et al.*, 2012), indicating that it efficiently inactivates Parp1 (**Fig. S2B,** quantified in **D**). Supplementation of 3-AB in the fly food also caused nucleolar fragmentation in epithelial tissue (**Fig. S2C**, quantified in **D**), indicating that the inhibitor is bioactive and was well tolerated (**Fig. S2E**).

Having established that our pharmaco-genetic manipulations are effective in wing disc cells, we proceeded to immunolocalize DNA damage foci using an antibody against the marker **γ**2HAv and apoptotic cells with an antibody against the marker cleaved Caspase 3 (cCas3). While control *MS>luc-RNAi* cells present no DNA damage foci, we observed that GFP-positive (GFP+) cells of *MS>SA1-RNAi* animals display a significant amount of DNA damage. Similar results were obtained in *MS>Parp1-RNAi* animals, or in $SA1^{ex86}$/+ animals, which are heterozygous for a *SA1* loss of function allele, indicating that the phenotype is not due to off-target effects (**Fig. 2B**, quantified in **C**). Interestingly, *Parp1-RNAi* GFP+ cells that are also depleted or heterozygous for *SA1* display more DNA damage foci, when compared to single manipulations (**Fig. 2B**, quantified in **C**). These data suggest that combined reduction of *SA1* and *Parp1* leads to an additive effect on DNA damage *in vivo*.

To determine whether the observed DNA damage is associated with Caspase-dependent apoptotic cell death, we also quantified the GFP+ cCas3+ cells. While control *MS>luc-RNAi* or *MS>Parp1-RNAi* cells present only occasional cCas3 staining, we observed that *MS>SA1-RNAi* or $SA1^{ex86}$/+ cells display a significant amount of cCas3 signal (**Fig. 2D,** quantified in **E**). These data suggest that reduced *SA1* expression, but not reduced *Parp1* expression, causes Caspase-dependent apoptotic cell death. Consistent with this, when combining reduced *SA1* and *Parp1* expression, no additional Cas3+ signal is observed *in vivo* (**Fig. 2D,** quantified in **E**). A similar pattern is observed upon quantification of the few cells per disc that are double positive for DNA damage foci and cCas3 expression (**Fig. 2F**).

Together, these data suggest that cells with reduced *SA1* and *Parp1* expression present high level of DNA damage and that a certain proportion of cells with reduced *SA1* expression are likely eliminated by Caspase-dependent apoptosis.

Consistent with the alterations observed in the larval wing pouch, *MS>SA1-RNAi* adult animals display curled wings, some of which with blisters (**Fig. S3A,** quantified in **B**). When compared with *MS>SA1-RNAi* animals, *MS>SA1-RNAi, Parp1* animals display a slight statistically significant reduction of the frequency of the animals with blisters (**Fig. S3B**). Slight amelioration of the wing phenotype was also observed upon feeding 3-AB to *MS>SA1-RNAi* animals (**Fig. S3C**). Wings appear normal in *MS>luc-RNAi* animals, $SA1^{ex86}$/+ animals, *MS>Parp1-RNAi* animals, *MS>Parp1-RNAi*, $SA1^{ex86}$/+ animals, or in *MS>luc-RNAi* animals that have been fed 3-AB (**Fig. S3A-B**), indicating that Parp1 inactivation or halving *SA1* dosage do not *per se* or combined affect wing development. These *in vivo* data suggest that the reduction of *Parp1* might modify the defects of *SA1*-depleted animals.

Cohesin activity is tumor suppressive during gliomagenesis

To assess the contribution of cohesin genes to brain tumorigenesis *in vivo*, we employed a genetic model of gliomagenesis based on expression in developing larval glial cells of constitutively active forms of *Drosophila* EGFR and of the PI3K homolog Pi3K92E/Dp110 (Read *et al.*, 2009), and of mC8GFP to mark the glial tissue **(Fig. 3A;** *repoGFPEP>* hereafter). To assess the effects of cohesin activity on glia cell development independent of tumorigenesis, we first depleted 5 cohesin genes *SA1, SMC1, SMC2, NippedB, Vtd* and *Mau2* individually in control glia expressing mCD8::GFP (*repoGFP>* hereafter). Compared to expression of a mock hairpin targeting *luciferase* (*repoGFP>luc-RNAi*), we did not observe major changes in CNS tissue growth at 120 hours after egg laying (AEL), with the exception of depletion of *Mau2*, which slightly reduced growth (**Fig. S4A**, quantified in **B**). When compared to *repoGFP>luc-RNAi* animals, *repoGFPEP>luc-RNAi*

animals at 120 hours AEL display a moderate CNS overgrowth that can be used as a sensitized background to evaluate the effect of further genetic modulations (**Fig. S4C**, quantified in **B).** Interestingly, depletion of the cohesin genes *SA1, SMC1* and *SMC3* in *repoGFPEP* animals led to increased CNS size and caused earlier lethality, when compared to *repoGFPEP>luc-RNAi* animals (**Fig. S4C**, quantified in **B**; **Fig. S5**).

We next assessed the effect of Parp1depletion of the phenotypes described above. Relative to control *repoGFP>luc-RNAi* and to *repoGFP>SA1-RNAi* animals, *repoGFP>Parp1-RNAi* or *repoGFP>Parp1-RNAi SA1-RNAi* animals display reduced CNS size, indicating that Parp1 is required to support CNS growth (**Fig. 3B,** quantified in **D**). Remarkably, a similar reduction of CNS size is observed in *repoGFPEP* animals, indicating that *Parp1* inactivation can fully revert the effects of reduced SA1 activity (**Fig. 3C,** quantified in **D**).

To investigate the origin of the effects described above, we labeled the nuclei of the glial cells with an antibody against Repo, and the cells undergoing caspase-dependent apoptosis with anti-cCas3 (**Fig. 3E-I**). In control glia, we observe that depletion of *SA1* slightly increased the number of glial nuclei (**Fig. 3E,** quantified in **G**), while depletion of *SA1, Parp1,* or both, leads to recovery of a significant amount of cCas3+ cells (**Fig. 3E,** quantified in **H**). Similar recovery of cCas3+ cells is observed in the CNS of animals bearing glial tumors (**Fig. 3F,** quantified in **H**). In glial tumors, depletion of *SA1* does not cause an increase in the number of Repo+ nuclei (**Fig. 3F,** quantified in **G**), but their nuclear size was found increased (**Fig. 3F,** quantified in **I**). Interestingly, *Parp1* depletion reduced the nuclear size of *SA1*-depleted glial cells, compared to that of *SA1*-depleted glial cells (**Fig. 3F,** quantified in **I**).

Overall, these data suggest that some cohesin genes, among which *SA1,* act as tumor suppressors and that *Parp1* activity is required to support the tissue growth caused by the reduction of *SA1* expression. These effects appear to correlate with glial nuclear size (compare **Fig. 3D** with **I**), rather than glial cell number or apoptosis, possibly suggesting an effect on cell size.

SA1 depletion during development leads to retention of undifferentiated cell masses in the adult brain

To further analyze the role of *SA1* in brain tumorigenesis, we used a genetic background that drives gene expression in larval NBII (Neumüller *et al.*, 2011), the 8 neural stem cells (NSC) that generate both neurons and glia of the posterior part of each hemisphere of the larval fly brain (**Fig. 4A**). In control animals at 120 AEL, NBII drives expression of mCD8::GFP to mark the NBII lineage and of a mock hairpin targeting *luciferase* (*NBII>luc-RNAi*). Depletion of the tumor suppressor *brat* (*NBII>brat-RNAi*) led to a massive increase in the number of NBII clusters. In contrast, expression

of the human brain tumor oncogene *NMYC* (*NBII>NMYC*), *SA1* heterozygosity *(NBII SA1^{86}/+)* or depletion of *SA1 (NBII>SA1-RNAi)*, or the combination of the two manipulations (*NBII>NMYC SA1-RNAi)*, do not significantly alter NBII numbers (**Fig. 4B,** quantified in **C**), indicating that *SA1* reduction does not increase NBII numbers.

To visualize dividing cells in NBII cluster, we immunolabeled with anti-phospho-Histone H3 (pHis3). We did not observe a large variation in the number of proliferating cells upon depletion of *brat*, or over expression of NMYC, while depletion of SA1 significantly reduced the number of proliferating cells (**Fig. S6A,** quantified in **B**). In *NBII>NMYC*, *NBII>NMYC SA1-RNAi* or *NBII>SA1-RNAi* animals, we occasionally observed the formation of aberrant mitotic figures, a defect not observed in control *NBII>luc-RNAi* or animals or *NBII>brat-RNAi* animals (**Fig. S6A**). These data suggest that *SA1* depletion does not promote proliferation of NBII.

NBII expression is known to abate with full maturation of neuroblast clusters at the end of pupal life. In agreement with this, we never recovered GFP+ cells persisting in the adult brain of *NBII>luc-RNAi* animals (**Fig. 4D,** quantified in **I**). Thus, we wondered whether our manipulations could lead to persistence of GFP+ cells in the brain, as previously reported for tumorigenesis mediated by loss of *brat* (Hadjipanayis and Brat, 2017; Reichardt *et al.*, 2018). Consistent with this, all *NBII>brat-RNAi* animals presented masses of GFP+ cells covering a large part of their adult brain (**Fig. 4E,** quantified in **I**). Interestingly, the occasional presence of GFP+ cells covering a small and highly variable part of the adult brain was also observed in *NBII>NMYC, NBII>NMYC SA1-RNAi* or *NBII>SA1-RNAi* animals (**Fig. 4F,** quantified in **I**). In adult brains, GFP+ masses are never recovered in *NBII>Parp1-RNAi* animals (**Fig. 4G,** quantified in **I**). The same result was observed by co-depletion of *Parp1* and of *SA1* (**Fig. 4H,** quantified in **I**), suggesting that Parp1 activity is required for persistence of the masses.

To test the levels of apoptosis upon *SA1* and *Parp1* depletion in NBII, we compared animals at 120 AEL. We observed that in control *NBII>luc-RNAi* animals, no cCas3+ cell was ever recovered (**Fig. S6C**). In contrast, a variable proportion of cCas3+ cells was recovered in *NBII>Parp1-RNAi*, *NBII>SA1-RNAi* or *NBII>Parp1-RNAi SA1-RNAi* clusters (**Fig. S6C**).

Overall, these data indicate that the reduction of *Parp1* activity prevents the formation of masses caused by reduced *SA1* expression, possibly by apoptotic elimination.

PARP inhibition improves neuroblast differentiation and lifespan in *SA1* knock-down flies

The emergence of NSC-derived undifferentiated brain cells in *SA1*-depleted adults might result from altered differentiation of larval NBII clusters. To analyze their state at 120 AEL, we immunolocalized Miranda (Mira), a marker of the intermediate neural precursors (INP) derived

from stem cell, Prospero (Pros), a marker of ganglion mother cells (GMC) that are produced by mature INPs, and Elav, which marks differentiated neurons in L3 larvae (**Fig. 5A**). In control *NBII>luc-RNAi* animals, we observed the expected distribution of Mira-, Pros- and Elav-positive cells emerging from GFP+ clusters. In sheer contrast, *NBII>SA1-RNAi* clusters accumulate Mira-positive cells at the expense of Pros- and Elav-positive cells. Similar results were obtained in $SA1^{ex86}$/+ animals (**Fig. 5B**, quantified in **D**). These data suggest that reduced *SA1* expression *per se* delays the transition of INP to GMC.

We next tested whether NBII differentiation is altered by the reduction of *Parp1* activity. In *NBII>Parp1-RNAi* NBII clusters, we observed a slight increase in Mira-positive cells but no change in Pros- and Elav-positive cells, when compared to *NBII>luc-RNAi* controls (**Fig. 5C**, quantified in **D**), suggesting that decreased Parp1 activity causes only a minor alteration of NBII differentiation. Remarkably, downregulation of *Parp1* ameliorated the NBII differentiation defect observed in *SA1*-depleted or $SA1^{ex86}$/+ animals (**Fig. 5C**, quantified in **D**). To determine whether inactivation of Parp1 during NBII differentiation could also be achieved pharmacologically, we fed animals with 3-AB. Consistent with our genetic data, we observed that 3-AB supplementation *per se* does not affect NBII differentiation. However, it partially phenocopies the effect of *Parp1* depletion, with amelioration of Pros- and Elav-positive cell differentiation (**Fig. 5E**). These results suggest that SA1 supports neuroblast cluster development and that the defects observed upon *SA1* reduction are rescued by impairment of PARP activity.

Despite the overall morphology of control, *SA1*-downregulated and *SA1* heterozygous animal adult brain appears unaffected (**Fig. S7**), we observed that *NBII>SA1-RNAi* animals display a 17% reduction in median survival, when compared to *NBII>luc-RNAi* animals. Similar data were obtained in control animals heterozygous for a null *SA1* allele (*NBII* $SA1^{ex86}$/+; **Fig. 5F**). Consistent with the effect on NBII differentiation, while 3-AB supplementation did not significantly alter the lifespan of control *NBII>luc-RNAi* animals, it improved the lifespan of animals with reduced *SA1* expression (**Fig. 5G**). The rescuing effect obtained by 3-AB supplementation was not observed on *NBII>brat-RNAi* animals (**Fig. 5F-G**).

Overall, we find that the reduction of PARP activity counteracts the tumor-associated effects of SA1 downregulation.

DISCUSSION

Database analyses highlighted a possible role of STAG2 in brain tumors, particularly in glioblastoma and medulloblastoma. As reported variants are predicted to result in STAG2 haploinsufficiency, we exploited an *in vitro* and *in vivo* system for modelling the contribution of reduced *STAG2* activity to relevant processes. Using HEK-293T cells with stable downregulation of

STAG2 as a human non-transformed 2D and 3D *in vitro* model, we first observed accumulation of DNA damage. Interestingly, when we exposed depleted cells to PARP inhibitors, we detected a statistically significant increase in cell death relative to baseline levels, suggesting the possibility of additive or synthetic lethal effects when both *STAG2* and PARP activity are reduced. To test the *in vivo* relevance of our *in vitro* data, we took advantage of pharmacogenetic manipulation of cohesin and PARP activity in *Drosophila melanogaster*. Based on depletion or heterozygosity of the fly *STAG2* homolog *SA1* and/or depletion of *Drosophila Parp1* (or inhibitor supplementation), we confirm the presence of DNA damage, as well as cell death in multiple tissues. We also reveal that cohesin genes and in particular *SA1* act as tumor suppressor in flies. In particular, we report for the first time that *SA1* depletion or heterozygosity is sufficient to delay, and possibly occasionally derail, terminal differentiation of brain stem cells and that *SA1* depletion promotes tissue growth in a model of gliomagenesis. Stinkingly, these tumor-relevant phenotypes are reverted by depletion or inhibition of PARP activity. We also find presence of caspase 3 activation in most tissues analyzed upon *SA1* or *Parp1* (or their combined) depletion. While this correlation implies a causation remains to be determined (see model in **Fig. 5H**).

A recent study in *Drosophila* has found that the sole alteration of epigenetic regulation of chromatin by impairing Polycomb activity is sufficient to promote tumorigenesis by changing genetic programs in the absence of driver mutations (Parreno *et al.*, 2024). Consistent with this, we observe delays in NBII differentiation and spontaneous retention of stem cell-derived masses in the fly adult brains. Thus, the regulation of chromatin architecture could be an important function of cohesin proteins relevant to tumor suppression. In favor of this, we also observe that *SA1* depletion mostly impacts nuclear - and possibly cell - size during gliomagenesis. These alterations might well be the result of the concerted changes in gene expression typical of altered chromatin regulation. However, in fly tissues upon *SA1* downregulation, we also observe accumulation of DNA damage, formation of defective mitotic figures and apoptosis, together suggesting that the effects of SA1 impairment are pleiotropic. Separation of function mutations will be required to attach to each cohesin function the correct tumorigenic potential. Interestingly, in different tissues we observe slightly different effects of the reduction of *SA1* expression and quantitatively different interactions with PARP inactivation, indicating that the effects of cohesin loss and PARP activity might be highly context dependent.

In neural stem cells, we conclude that correct *SA1* expression supports neuroblast differentiation during larval life and prevents the persistence of NBII-derived masses. While these masses in adult brains are occasional, and we have not yet characterized their nature, cohesin genes have been implicated in axonal pruning (Schuldiner *et al.*, 2008), suggesting defects in post mitotic elimination of persistent NBIIs. *SA1* depletion has also been recently shown to increase the

migration of tumor cells of epithelial origin in flies (Canales Coutiño *et al.*, 2020). Thus, it will be interesting to study also whether the brain masses observed in our experiments have migrated away from sites of NBII development.

Precise control of NB cell elimination during embryonic nervous system development depends on *SA1* activity, downstream of the H3K27me3 chromatin state modulation of by Notch (Arya *et al.*, 2019). Remarkably, epigenetic regulation by Polycomb proteins increases the activity of stemness genes during asymmetric cell division of NBII by elevating H3K27me3 levels at cis-regulatory elements in INP cells. These authors suggest that a failure of this process could reduce Notch activity and thereby promote INP proliferation instead of maintaining their stemness (Rajan *et al.*, 2023). In this context, Notch activity is also known to be repressed by the tumor suppressor Brat (human TRIM3) to promote differentiation of immature neural precursors (Hadjipanayis and Brat, 2017). Consistent with this, the masses observed in adult fly brain with reduced NSC expression of *SA1*, resemble those more abundantly obtained upon *brat* depletion. Thus, it would be interesting in the future to assess whether *SA1* reduction alters Notch regulation of NBII development.

How do the differentiative phenotypes discussed above correlate with DNA damage and cell death? At present, our correlative data do not clarify whether the accumulation of DNA damage and activation of cell death contribute to or hinder tumorigenesis. However, such phenotypes are reminiscent of those reported in response to replication stress upon cohesin removal, or PARP inhibition, or oncogenic MYC activity (Colicchia *et al.*, 2017; Benedict *et al.*, 2020; Peripolli *et al.*, 2024). Consistent with this, we observed the occasional presence of persistent masses derived from NBII cells also in the fly brain overexpressing NMYC. In epithelial tissue, PARP inhibition *per se* is sufficient to cause accumulation of DNA damage; in addition, the combination of PARP inhibition and reduction of *SA1* expression results in a synergistic effect. However, *in vivo* we do not observe the synthetic lethality suggested by *in vitro* experiments. This discrepancy might depend on the complex relations entertained by cells in a tissue context. Despite this, our *in vitro* and *in vivo* results are in line with reports that glioblastoma cells with *STAG2* mutations show an increase in DNA damage markers and cell cycle arrest caused by replication stress when treated with PARP inhibitors (McLellan et al. 2012; Tothova et al. 2013; Bailey et al. 2020) and with a clinical trial exploring PARP inhibition in blood cancers with mutations in cohesin genes (https://clinicaltrials.gov/study/NCT03974217). Moreover, they suggest that the radiation sensitivity observed upon PARP inhibition in *in vitro* models of certain types of medulloblastoma (Price and Lau, 2023) might involve cohesin activity.

Overall, we have laid the groundwork for future in-depth analysis of the combined effects of reduced cohesin activity and PARP inhibition in a practical, inexpensive, and 3R-compliant set of *in*

vivo models of brain development and tumorigenesis. Further study of these models will yield an understanding of how to harness PARP inhibition to revert the effects of reduced cohesin activity in cancer.

MATERIAL AND METHODS

Cell cultures and cell-based assays

HEK-293T cells were grown in DMEM medium (Dulbecco's modified Eagle's medium, Life technologies, 11965092) supplemented with 10% FBS (fetal bovine serum, Life technologies, 10500064) and 1% of penicillin-streptomycin (P/S) (Euroclone, ECB3001D). Cells were cultured in a Petri dish at 5% CO2 and 37 °C.

HEK-293T shSCR and HEK-293T shSTAG2 are derived from HEK-293T control (CTRL) cell line obtained through viral infection with a control scrambled (SCR) plasmid and the one containing a short hairpin (sh) for the STAG2 gene silencing (shSTAG2); both plasmids also contain GFP encoding gene and puromycin cassette for selection. Briefly, STAG2-shRNA lentiviral vector (Origene, Locus ID 10735) or the control scrambled (SCR) sequence SCR-shRNA as well as packaging and envelop virus components was transfected into HEK-293T cells by using $CaCl_2$ method. After two days, media containing virus particles were collected and used to infect new HEK-293T cells to generate stable cell lines. Cells were positively selected with puromycin (1ug/mL Invivogen ANT-PR-5) treatment for 72 hours (h) 48h post-infection, and then periodically maintained under selection.

To perform MTT assays, 20000 cells/well were seeded in a 24 multiwell till 70% of confluence. Then, the culture medium was removed, and 300µl of serum-free blank medium and 30µl of MTT stock solution (5mg/ml MTT powder Sigma-Aldrich, M2003) were added to each well. The plate was incubated at 37°C for 30min/2 hours until purple precipitates appear. After removing the solution, 300ul of isopropanol were added to each well, and the plate was shaken for 10 minutes at RT. After resuspension, 200µl of each well were transferred into a 96 multiwell with lid. The levels of precipitates were read by Insite spectrophotometer at 570nm.

For adhesion tests, cells in triplicates were seeded at a concentration of 40.000 cells per well in a 24 well plate containing a glass slide, then the plate was incubated for 2 hours at 37°C. After medium removal, cells were fixed with 300µl of cold methanol for 10 minutes at -20°C. After fixation each well was washed twice with PBS 1X for 5 minutes and 300µl of hematoxylin were added for 1 minute at RT. After hematoxylin removal, each well was washed with water until it

became clear and 300µl of eosin were added for 1 minute at RT. Each well was washed with water and slides were mounted on a slide with Mowiol.

To assess spheroid formation, 5000 cells/well were seeded in a low attachment 96 U-bottom multiwell. Cells were resuspended in DMEM/F12 medium (Gibco, 11320033) containing B-27 supplement (100X, Gibco, 12587010), N-2 supplement (50X, Gibco, 17502048), heparin (2 µg/ml, Merck Life Science, H3149-50KU), EGF (20 ng/mL, Prepotech, AF-100-15-500UG), FGF2 (10 ng/mL, Prepotech, AF-100-18B-500UG), and P/S 100X. Then, 200ul/well were aliquoted and the plate was centrifuged for 5 min at 300g. Spheroids of each cell line were grown for 4 days and then moved to a 24 well plate previously coated with Matrigel (Merck Life Science, CLS356234-1EA) to evaluate dissemination ability.

For PARP inhibition, shSCR and shSTAG2 HEK-293T cells and 4 day-old spheroids were treated with 3-Aminobenzamide (3-AB) at 500uM for 72 hours and then fixed for further experiments. An equal volume of DMSO was used as a vehicle control.

The terminal deoxynucleotidyl transferase dUTP and labeling assay (TUNEL) was performed on fixed HEK-293T cell using the *in situ* cell death detection AP kit (Roche 11684809910) according to the manufacturing instructions. Slides were mounted with Mowiol and images were acquired at the microscope.

Drosophila methods

Drosophila strains were maintained in vials containing a standard food medium composed of water, 34% cornmeal, 57% molasses, 9% yeast, 0.7% agar, 0.7% propionic acid and 2% tegosept. Supplemented food composition was modified by replacing molasses with 35% sucrose and with 44% yeast concentration to enhance egg-laying. Unless otherwise specified, fly lines were generated by crossing or recombination from stocks obtained in our laboratory or sourced from the Bloomington Drosophila Stock Center (BDSC), Indiana University, and the Vienna Drosophila Resource Center (VDRC). Crosses were kept at 25°C. The following fly stocks were used:

Code	Origin	Genotype
64349	BDSC	*CantonS*
31603	BDSC	*y[1] v[1];+; P{y[+t7.7] v[+t1.8]=TRiP.JF01355}attP2*
	This Work	*w118, ms1096Bx-GAL4,P{w[+mC]=UAS-EGFP}8; +; +*
	Cédric Maurange, Aix Marseille University	*UAS-dicer2;wor-GAL4, ase-GAL80/;UAS-mCD8::GFP*
36794	BDSC	*y[1] sc[*] v[1] sev[21]; P{UAS-TRiP.GL00534}attP40/CyO,Tb; +*
33395	BDSC	*y[1] sc[*] v[1] sev[21]; +; P{y[+t7.7] v[+t1.8]=TRiP.HMS00272}attP2*
	McKim, The State University of New Jersey	*+, SA[ex86] pr FRT40A / CyO; +*
	This Work	*+; P{UAS-TRiP.GL00534}attP40/CyO,Tb;P{GD9445}v46745*
	This Work	*+; SA[ex86] pr FRT40A/CyO,Tb;P{GD9445}v46745*
46745	VDRC	*w1118;+;P{GD9445}v46745*
	Renee Read, Emory University	*UAS DP110-CAAX; +; Repo GAL4-UASmCD8GFP,UAS ΔEGFRλ/TM6c,Tub-GAL80*
	Renee Read, Emory University	*+; +; Repo GAL4-UASmCD8GFP/TM2*
65229	BDSC	*y[1] sc[*] v[1] sev[21];P{y[+t7.7] v[+t1.8]=TRiP.HMC06090}attP40; +*
36598	BDSC	*y[1] sc[*] v[1] sev[21]; +; P{y[+t7.7] v[+t1.8]=TRiP.GL00558}attP2*
36783	BDSC	*y[1] sc[*] v[1] sev[21]; P{y[+t7.7] v[+t1.8]=TRiP.GL00518}attP40; +*
36794	BDSC	*y[1] sc[*] v[1] sev[21]; P{TRiP.GL00534}attP40 / CyO; +*
41976	BDSC	*y[1] sc[*] v[1] sev[21]; +; P{y[+t7.7] v[+t1.8]=TRiP.HMS02374}attP2*

For *in vivo* PARP inhibitor supplementation, 3-AB (Catalog No. S1132, Selleck USA) was used as PARP inhibitor. To establish an effective and non-toxic dose, a 50 mM stock solution was prepared in DMSO following manufacturer's datasheet and diluted in sterile distilled water to concentrations of 5–250 µM. 150 µL of each of these were added to a culturing tube containing 3 mL of *Drosophila* white food, pre-punctured with 20 holes for uniform diffusion. Equal volumes of DMSO diluted in distilled water served as controls. For all other treatments, animals were reared in tubes containing food supplemented with a final concentration of 2.5 µM 3-AB or vehicle (DMSO). In lifespan experiments, cohorts of 20 flies/genotype (10 males and 10 females) per vial were kept at 25°C. Flies were transferred to fresh food medium every two to three days, when dead flies were also scored.

In gliomagenesis and neuroblast experiments, animals were synchronized by short times of egg deposition and larvae were collected, at 120 hours AEL dissected and processed for immunofluorescence. For the estimation of pupal lethality, tubes previously cleared of parentals after egg deposition were analyzed after 25 days of culturing. At the time of analysis all the viable offsprings were removed and the dead animals found in the tube were categorized according to their appearance: animals dead before pupariation that have crawled up the tube or that are visible as L3 in the food (L3 lethality). Dead animals that have

pupariated in which no metamorphosis has occurred (Early pupa). These appear as pupal cases that have not eclosed filled with dried clear tissue. Dead animals that have pupariated and that present signs of metamorphosis, such as blackened eyes or wings (Late pupa).

Adult brains were dissected from 7-10 day-old animals and processed for immunofluorescence.

Real-time quantitative PCR

For cell culture experiments, 1µg of RNA extracted with phenol/chloroform method by NucleoZOL (Macherey-Nagel) was retrotranscribed by using All-In-One 5X RT MasterMix (Microtech) kit. Quantitative real-time PCR (RT-qPCR) TB Green Premix Ex Taq (Tli RNase H Plus) (Takara) kit and the CFX Opus 96 Real-Time PCR System (Bio-Rad) were used to evaluate gene expression following manufacturer instructions. The data obtained from RT-qPCR were analyzed using a comparative Ct quantification method. ΔCt was obtained by normalizing each Ct sample to the housekeeping genes (*GAPDH, RPLP0, RPL13A*) mean. Then the ΔΔCt was obtained by comparing the ΔCt of every sample for each gene to the reference one gene expression of the treated samples against their control. Relative gene expression values were obtained by calculating the fold change, which corresponds to 2^ -ΔΔCT). Technical and biological triplicates were performed for all the experiments. The following primers were used for RT-qPCR:

GAPDH (For: 5'-AGCCACATCGCTCAGACAC; Rev: 5′- GCCCAATACGACCAAATCC)

RPLP0 (For: 5'- TCTACAACCCTGAAGTGCTTGAT; Rev. 5′- CAATCTGCAGACAGACACTGG)

RPL13A (For: 5'- CCTGGAGGAGAAGAGGAAAGAGA; Rev: 5′- TTGAGGACCTCTGTGTATTTGTCAA)

STAG2 (For: 5'- AAGGAGGACTTGCTGCGTTT; Rev. 5′- TCCTCTTGCTGACCATCTGC). RT-qPCR and western blot data were performed using Student t-test.

For *in vivo* experiments, after dissection, organs of the selected genotype were homogenized in Trizol reagent (Invitrogen, 15596-018). For wing disc 30 discs were used.

The RNA extraction was performed using a commercial kit (Kit Zymo RNA extraction insect tissue). The concentration of extracted RNA and DNA were measured using the NanoDrop 1000 Spectrophotometer. Retrotranscription of RNA to cDNA was performed using LunaScript® RT SuperMix Kit (New England BioLabs, E3010). RT-qPCR was performed with Luna® Universal qPCR Master Mix (New England BioLabs, M3003) by using the CFX Connect Real Time PCR Detection System (Bio-Rad, 1855201).

Results were normalized using the housekeeping *Rp49* and the ΔΔ cycle threshold method and results expressed as the relative change (-fold) of the downregulated group over the control group, which was used as a calibrator.

GFP, *SA* and *Rp49* RT-qPCRs were performed using Sybergreen (Applied Biosystems) with the following primers:

*SA (*F: 5'- TTGTGCGACACTCGAAGAAC; R: 5'- CCGCTTTCTTCGTCAAACTC),

*Rp49 (*F: 5′-ACGTTGTGCACCAGGAACTT; R: 5′-TACAGGCCCAAGATCGTGAA).

Output data were analyzed using CFX Manager Software (BioRad) and Prism that was used also to realize graphs.

Protein extraction and quantification and Western blot and analysis

For cell extracts, HEK-293T pellets were resuspended in cold S300 buffer (NaCl 300mM, HEPES pH 7.6 50mM, NP40 0,1%, MgCl2 2mM, glycerol 10%) added with protease and phosphatase inhibitors and GENIUSTM Nuclease (SC-202391). Samples were left on ice for 1 hour and then centrifuged at maximum speed for 10 minutes at 4°C. Supernatants containing protein lysates were collected and quantified using Bradford method. BSA 0,2mg/ml (Bio-rad 5000206) was used to prepare the standard curve. Finally, samples were predisposed for the western blot run by preparing aliquots at 1µg/µl supplemented with Laemmli sample buffer 4x (LSB)(Bio-Rad, 1610747) and boiled for 10 minutes at 100°C. 30µg of samples were loaded and separated by SDS-PAGE (Running buffer 1x diluted from 10x made of 3% Tris HCl, 14,4% Glycine and 1% SDS) using 10% polyacrylamide gels (Biorad Mini-PROTEAN TGX Gels, 4561034). At the end of the run, cold transfer buffer 1X (20% methanol and 10% Transfer buffer 10x, composed of 3% Tris HCl and 14,4% Glycine) was used to transfer protein samples to a nitrocellulose membrane (Merck Life Science, GE10600003). Milk (Sigma-Aldrich, 4259001) 5% in TBS-T 1X was used as a blocking solution for 1h at RT, then membranes were incubated with primary antibody diluted in milk or TBS-T 1X at 4°C O/N (rabbit anti-STAG2, 1:1000, Cell Signaling, 5882; rabbit anti-γH2A.X, 1:1000 Cell signaling, BK9718S; rabbit anti- GAPDH 1:1000, Cell signaling, 5174). Then, membranes were incubated with secondary antibody anti-rabbit or anti-mouse HRP 1:3000 (Biorad, rabbit 1706515, mouse 1706516) diluted in TBS-T 1X or in milk for 1h at RT. Membranes were washed three times with TBS-T 1X and incubated with ECL or Amersham to detect chemiluminescence signals captured by Chemidoc Imaging System.

Immunofluorescence analyses

Cells were permeabilized for 10' with PBT (PBS with 0,25% Triton) and then natural donkey serum (20% of NDS in PBT 0,25%) was used as blocking solution for 1h at RT. Cells were incubated with primary antibody rabbit anti-γH2AX (1:200, Cell signaling, BK9718S), and rabbit anti-cCas3 (1:200, Cell signaling, BK9664S) at 4°C overnight. The day after, secondary antibodies donkey Alexa Fluor Cy-3- conjugated anti-rabbit Fab fragments (1:200; Jackson Immunoresearch) were used and incubated for 2 hours at RT. Then, cells were washed with PBT 0,25% three times and DAPI (1:1000) was used for nuclei counterstaining. Finally, cells were washed with PBS 1X and with MilliQ water. Slides were mounted with Mowiol (Sigma Aldrich), and signals were acquired by fluorescence microscope at a 10x magnification and for cCas3 quantified by ImageJ software.

For immunolabeling of *Drosophila* organs, adult brain were dissected and processed as described (Wu and Luo, 2006; Ostrovsky, Cachero and Jefferis, 2013). Larvae were reared for 120–150 hours post-egg deposition and wandering third-instar larvae were selected for analysis. Larval brains and wing discs remained attached to carcasses for ease of handling. Carcasses were prepared by removing the gut, fat tissue,

and salivary glands in 1× PBS, then fixed in 4% PFA for 20 min at room temperature. Tissues were rinsed three times in 0.1% Triton X-100 in 1× PBS (PBST) for 5 min to remove fixative, followed by permeabilization in 0.3% Triton X-100 in 1× PBS (PBST 0.3%) for 30 min. Blocking was performed with 5% BSA in PBST 0.3% for 30 min before overnight incubation with primary antibodies diluted in blocking solution. The following primary antibodies were used: chicken anti-GFP (1:1000, Abcam, 92456), rabbit anti-Miranda (1:500, Abca, 197788), mouse anti-Prospero (1:100, DSHB, 528440), rat anti-Elav (1:50, DSHB, 528218), mouse anti-histone 2A gamma variant, phosphorylated (γH2Av) (1:50, DSHB, 2618077), rabbit anti-Fibrillarin (1:500, Abcam, 5821), mouse anti-nc82 (1:40, DSHB, 2314866), rabbit anti-cCas3 (1:200, Cell Signalling Technology, 9661), mouse anti-pH3 (1:2000, Abcam,14955) and mouse anti-Repo (1:200, DSHB, 528448). After three washes, Alexa Fluor-conjugated secondary antibodies (1:300, Invitrogen) were incubated for 2 hours at room temperature. DNA was stained with DAPI (1:5000, Sigma Aldrich), followed by three washes and fine dissection. Samples were mounted in Mowiol (Sigma Aldrich) and dried overnight at room temperature.

Microscope acquisition

Brightfield images of 2D cell plates were acquired with 40X magnification, while 3D spheroids were acquired with 4X magnification. Confocal images were acquired with a Nikon A1R/AX laser scanning confocal microscope equipped with a Nikon A1/AX plus camera and the following objectives (Nikon): Plan Fluor 10X DIC L N1 (NA 0.3), Plan Fluor 20X DIC N2 (NA 0.5); DAPI, Alexa Cy3 were excited at 405, 561 nm and observed at 425–475, 570–620 nm, respectively.

Images of *Drosophila* organs were acquired using Nikon A1-SIM or NiU confocal microscopes from the UniTECH NoLimits departmental platform (https://unitech.unimi.it/) at varied magnifications. Immunofluorescence images were analyzed using FIJI software FIJI (Fiji is just ImageJ, NIH), followed by statistical analysis with Prism (GraphPad software version 9.1.2 La Jolla, CA, USA; www.graphpad.com). Measurements and fluorescence evaluation were carried out through the FIJI Software. Quantification analysis was performed by evaluating equal numbers of Z-stack among different genotypes for comparative analysis.

Database searches

The publicly accessible cBioPortal for cancer genomics database (https://www.cbioportal.org/) was investigated, selecting datasets from 8 studies of medulloblastoma (Jones *et al.*, 2012; Pugh *et al.*, 2012; Robinson *et al.*, 2012; Poeran, 2016; Northcott *et al.*, 2017) and glioblastoma (Brennan *et al.*, 2013; Zhao *et al.*, 2019; Wang *et al.*, 2021). The CADD score, a numerical ranking that predicts the deleteriousness of a protein variant, was calculated using CADD v1.7 (https://cadd.gs.washington.edu/) for all SNP *STAG2* variants reported in gnomAD (https://gnomad.broadinstitute.org/) and the ones identified in cBioPortal. Patients belonging to two different datasets were considered only one time.

Quantifications

All cell culture experiments were performed in biological and technical triplicates. To quantify the cCas3 signal, the ImageJ software and the integrated raw density (IntDen) method was used (Shihan *et al.*, 2021). We counted four different fields and the integrated density for every field was calculated with an adjusted threshold of 183. For adhesion tests, three images for each well for each condition were acquired and cells were counted by ImageJ software. Then, the average of each replicate was normalized with the average of control cells for each experiment. Data obtained from western blots were analyzed using ImageJ software, and the mean pixel intensity was calculated. In the TUNEL experiment at least 3 images for each condition for each experiment were acquired. Cells were counted by ImageJ, and the ratio of TUNEL-positive cells over the total cells in a field was calculated.

In fly experiments, for the analysis of larval wing discs acquired at 20× magnification, a selection mask was created around the GFP-positive tissue to quantify surface area. For gliomagenesis analyses, the total brain area was quantified by drawing a ROI on the maximum projection of the entire brain (30–35 z-slices). For mid-section analysis, comparable single-plane images were acquired, the optic lobe area was selected with "Freehand selection", and the percentage of fluorescence per channel was measured by thresholding. For Repo/DAPI analysis, the intensity ratio between the two channels was calculated within the same selection. The number of Repo+ cells per lobe was obtained using the Cell Counter 2D plugin (Fiji). Repo+ nuclear areas were manually drawn (“Freehand selection”) in 20 cells per optic lobe and reported as mean value. For the measurements of GFP+ cell masses in adult brains, the GFP+ area was measured on a Max Projection of the full Z-stack using FIJI’s "Freehand Selection" tool and quantified with the "Measure" command. For immunofluorescence analysis of NBII a 10-slice Z-stack (0.2 µm per slice) was acquired for each sample. The GFP+ outer contour was outlined using the "Freehand Selection" tool, creating a ROI mask applied to individual fluorescence channels. The "Threshold" function defined positive signals relative to background, and the occupied area was measured as the percentage of pixels within the ROI.

All counts were analyzed with PRISM GraphPad software. The selected statistical test and sample size are shown in the figures or in the figure legends. In all analyses, significance is considered for p-values < 0.05 (ns $p>0.05$; * $p < 0.05$; ** $p < 0.01$; *** $p < 0.001$; **** $p < 0.0001$). Each sample was compared to sample 1 (control) and P-value intervals are reported above the value, unless otherwise noted. Non-significant comparisons (ns) are not indicated, unless when relevant. Other meaningful comparisons and relative P-value intervals are indicated with lines above the values connecting the samples compared.

ACKNOWLEDGEMENTS

The authors are thankful for the support of the microscopy facility NOLIMITS of the University of Milan and the Bloomington and Vienna *Drosophila* Stock Center. We are grateful to Cedric Maurange (Aix Marseille University) and Kim McKim (Rutgers University) for providing fly stocks.

COMPETING INTERESTS

The authors have no competing or financial interest.

AUTHOR CONTRIBUTIONS

TV and VM designed the study. ST conducted all the *Drosophila* experiments with the technical help of FL under the supervision of TV. AL and SC performed the experiments in human cells and the computational analysis under the supervision of CG and VM. TV and VM wrote the manuscript with the help of ST and AL.

FUNDING

ST acknowledges the support of the PhD school Translational Medicine of the University of Milan. AL is a postdoctoral fellow of Fondazione Veronesi and receives support from the linea 2 grant of the University of Milan. This work is also made possible by the AIRC (Associazione Italiana Ricerca sul Cancro) IG grant 20661 and WCR (Worldwide Cancer Research) Grant 18-399 to TV and by funds of the University of Milan to CG and VM.

DATA AND RESOURCE AVAILABILITY

All relevant data and details of resources can be found within the article and its supplementary information.

REFERENCES

Arruda, N. L. *et al.* (2020) 'Distinct and overlapping roles of STAG1 and STAG2 in cohesin localization and gene expression in embryonic stem cells', *Epigenetics and Chromatin*, 13(1). doi: 10.1186/s13072-020-00353-9.

Arya, R. *et al.* (2019) 'A Cut/cohesin axis alters the chromatin landscape to facilitate neuroblast death', *Development (Cambridge)*, 146(9). doi: 10.1242/dev.166603.

Bailey, M. L. *et al.* (2014) 'Glioblastoma cells containing mutations in the cohesin component STAG2 are sensitive to PARP inhibition', *Molecular Cancer Therapeutics*, 13(3), pp. 724–732. doi: 10.1158/1535-7163.MCT-13-0749.

Balbás-Martínez, C. *et al.* (2013) 'Recurrent inactivation of STAG2 in bladder cancer is not associated with aneuploidy', *Nature Genetics*, 45(12), pp. 1464–1469. doi: 10.1038/ng.2799.

Bayés, M. *et al.* (2001) 'Evaluation of the Stag3 gene and the synaptonemal complex in a rat model (as/as) for male infertility', *Molecular Reproduction and Development*, 60(3). doi: 10.1002/mrd.1104.

Benedict, B. *et al.* (2020) 'WAPL-Dependent Repair of Damaged DNA Replication Forks Underlies Oncogene-Induced Loss of Sister Chromatid Cohesion', *Developmental Cell*, 52(6). doi: 10.1016/j.devcel.2020.01.024.

Boamah, E. K. *et al.* (2012) 'Poly(ADP-ribose) polymerase 1 (PARP-1) regulates ribosomal biogenesis in Drosophila nucleoli', *PLoS Genetics*, 8(1), pp. 1–14. doi: 10.1371/journal.pgen.1002442.

Brennan, C. W. *et al.* (2013) 'The somatic genomic landscape of glioblastoma', *Cell*, 155(2). doi: 10.1016/j.cell.2013.09.034.

Brohl, A. S. *et al.* (2014) 'The Genomic Landscape of the Ewing Sarcoma Family of Tumors Reveals Recurrent STAG2 Mutation', *PLoS Genetics*, 10(7). doi: 10.1371/journal.pgen.1004475.

Canales Coutiño, B. *et al.* (2020) 'A Genetic Analysis of Tumor Progression in Drosophila Identifies the Cohesin Complex as a Suppressor of Individual and Collective Cell Invasion', *iScience*, 23(6), p. 101237. doi: https://doi.org/10.1016/j.isci.2020.101237.

Colicchia, V. *et al.* (2017) 'PARP inhibitors enhance replication stress and cause mitotic catastrophe in MYCN-dependent neuroblastoma', *Oncogene*, 36(33), pp. 4682–4691. doi: 10.1038/onc.2017.40.

Crompton, B. D. *et al.* (2014) 'The genomic landscape of pediatric Ewing sarcoma', *Cancer Discovery*, 4(11). doi: 10.1158/2159-8290.CD-13-1037.

D'Andrea, A. D. (2018) 'Mechanisms of PARP inhibitor sensitivity and resistance', *DNA Repair*, 71, pp. 172–176. doi: 10.1016/j.dnarep.2018.08.021.

Gause, M. *et al.* (2008) 'Functional links between Drosophila Nipped-B and cohesin in somatic and meiotic cells', *Chromosoma*, 117(1), pp. 51–66. doi: 10.1007/s00412-007-0125-5.

Guo, G. *et al.* (2013) 'Whole-genome and whole-exome sequencing of bladder cancer identifies frequent alterations in genes involved in sister chromatid cohesion and segregation', *Nature Genetics*, 45(12). doi: 10.1038/ng.2798.

Hadjipanayis, C. and Brat, D. J. (2017) 'Drosophila Brat and human ortholog TRIM3 maintain stem cell equilibrium and suppress brain tumorigenesis by attenuating Notch nuclear transport', *Cancer Res*, 76(8), pp. 2443–2452. doi: 10.1158/0008-5472.CAN-15-2299.Drosophila.

Hill, V. K., Kim, J. S. and Waldman, T. (2016) 'Cohesin mutations in human cancer', *Biochimica et Biophysica Acta - Reviews on Cancer*. doi: 10.1016/j.bbcan.2016.05.002.

Jones, D. T. W. *et al.* (2012) 'Dissecting the genomic complexity underlying medulloblastoma', *Nature*, 488(7409). doi: 10.1038/nature11284.

Kline, A. D. *et al.* (2018) 'Diagnosis and management of Cornelia de Lange syndrome: first international consensus statement', *Nature Reviews Genetics*. doi: 10.1038/s41576-018-0031-0.
Kon, A. *et al.* (2013) 'Recurrent mutations in multiple components of the cohesin complex in myeloid neoplasms', *Nature Genetics*, 45(10). doi: 10.1038/ng.2731.
De Koninck, M. and Losada, A. (2016) 'Cohesin mutations in cancer', *Cold Spring Harbor Perspectives in Medicine*, 6(12). doi: 10.1101/cshperspect.a026476.
Liu, Y. *et al.* (2018) 'Somatic mutation of the cohesin complex subunit confers therapeutic vulnerabilities in cancer', *Journal of Clinical Investigation*, 128(7), pp. 2951–2965. doi: 10.1172/JCI98727.
Luo, J. *et al.* (2024) 'An update on small molecule compounds targeting synthetic lethality for cancer therapy', *European Journal of Medicinal Chemistry*, 278, p. 116804. doi: 10.1016/J.EJMECH.2024.116804.
Maurange, C. (2020) 'Temporal patterning in neural progenitors: From Drosophila development to childhood cancers', *DMM Disease Models and Mechanisms*, 13(7). doi: 10.1242/dmm.044883.
Mekonnen, N., Yang, H. and Shin, Y. K. (2022) 'Homologous Recombination Deficiency in Ovarian, Breast, Colorectal, Pancreatic, Non-Small Cell Lung and Prostate Cancers, and the Mechanisms of Resistance to PARP Inhibitors', *Frontiers in Oncology*, 12. doi: 10.3389/fonc.2022.880643.
Mondal, G. *et al.* (2019) 'A requirement for STAG2 in replication fork progression creates a targetable synthetic lethality in cohesin-mutant cancers', *Nature Communications*, 10(1). doi: 10.1038/s41467-019-09659-z.
Mullegama, S. V. *et al.* (2017) 'De novo loss-of-function variants in STAG2 are associated with developmental delay, microcephaly, and congenital anomalies', *American Journal of Medical Genetics, Part A*, 173(5), pp. 1319–1327. doi: 10.1002/ajmg.a.38207.
Di Nardo, M., Pallotta, M. M. and Musio, A. (2022) 'The multifaceted roles of cohesin in cancer', *Journal of Experimental and Clinical Cancer Research*. doi: 10.1186/s13046-022-02321-5.
Nasmyth, K. (2011) 'Cohesin: A catenase with separate entry and exit gates?', *Nature Cell Biology*. doi: 10.1038/ncb2349.
Nasmyth, K. and Haering, C. H. (2009) 'Cohesin: Its roles and mechanisms', *Annual Review of Genetics*, 43, pp. 525–558. doi: 10.1146/annurev-genet-102108-134233.
Neumüller, R. A. *et al.* (2011) 'Genome-wide analysis of self-renewal in Drosophila neural stem cells by transgenic RNAi', *Cell Stem Cell*, 8(5), pp. 580–593. doi: 10.1016/j.stem.2011.02.022.
Northcott, P. A. *et al.* (2017) 'The whole-genome landscape of medulloblastoma subtypes', *Nature*, 547(7663), pp. 311–317. doi: 10.1038/nature22973.

Ostrovsky, A., Cachero, S. and Jefferis, G. (2013) 'Clonal analysis of olfaction in Drosophila: Generation of flies with mosaic labeling', *Cold Spring Harbor Protocols*, 8(4). doi: 10.1101/pdb.prot071712.

Paglia, S. *et al.* (2017) 'Failure of the PTEN/aPKC/Lgl axis primes formation of adult brain tumours in drosophila', *BioMed Research International*, 2017. doi: 10.1155/2017/2690187.

Parreno, V. *et al.* (2024) 'Transient loss of Polycomb components induces an epigenetic cancer fate', *Nature*, 629(8012). doi: 10.1038/s41586-024-07328-w.

Peripolli, S. *et al.* (2024) 'Oncogenic c-Myc induces replication stress by increasing cohesins chromatin occupancy in a CTCF-dependent manner', *Nature Communications*, 15(1). doi: 10.1038/s41467-024-45955-z.

Phan, A. *et al.* (2019) 'Stromalin Constrains Memory Acquisition by Developmentally Limiting Synaptic Vesicle Pool Size', *Neuron*, 101(1), pp. 103-118.e5. doi: 10.1016/j.neuron.2018.11.003.

Poeran (2016) 'Divergent clonal selection dominates medulloblastoma at recurrence', *Nature*, 176(12), pp. 139–148. doi: doi:10.1038/nature16478. Divergent.

Price, L. and Lau, B. (2023) 'MDB-36. SONIDEGIB, GANT61, AND VELIPARIB TREATMENT BOTH ALONE AND IN COMBINATION INCREASES RADIATION SENSITIVITY IN PEDIATRIC SONIC HEDGEHOG MEDULLOBLASTOMA', *Neuro-Oncology*, 25(Supplement_1), pp. i70–i70. doi: 10.1093/neuonc/noad073.268.

Pugh, T. J. *et al.* (2012) 'Medulloblastoma exome sequencing uncovers subtype-specific somatic mutations', *Nature*, pp. 106–110. doi: 10.1038/nature11329.

Rajan, A. *et al.* (2023) 'Low-level repressive histone marks fine-tune gene transcription in neural stem cells', *eLife*, 12. doi: 10.7554/eLife.86127.

Read, R. D. *et al.* (2009) 'A Drosophila model for EGFR-Ras and PI3K-dependent human glioma', *PLoS Genetics*, 5(2). doi: 10.1371/journal.pgen.1000374.

Reichardt, I. *et al.* (2018) 'The tumor suppressor Brat controls neuronal stem cell lineages by inhibiting Deadpan and Zelda', *EMBO reports*, 19(1), pp. 102–117. doi: 10.15252/embr.201744188.

Robinson, G. *et al.* (2012) 'Novel mutations target distinct subgroups of medulloblastoma', *Nature*, 488(7409). doi: 10.1038/nature11213.

Rollins, R. A. *et al.* (2004) ' Drosophila Nipped-B Protein Supports Sister Chromatid Cohesion and Opposes the Stromalin/Scc3 Cohesion Factor To Facilitate Long-Range Activation of the cut Gene ', *Molecular and Cellular Biology*, 24(8). doi: 10.1128/mcb.24.8.3100-3111.2004.

Romero-Pérez, L. *et al.* (2019) 'STAG Mutations in Cancer', *Trends in Cancer*, 5(8), pp. 506–520. doi: 10.1016/j.trecan.2019.07.001.

Schuldiner, O. *et al.* (2008) 'piggyBac-Based Mosaic Screen Identifies a Postmitotic Function for Cohesin in Regulating Developmental Axon Pruning', *Developmental Cell*, 14(2). doi: 10.1016/j.devcel.2007.11.001.

Shihan, M. H. *et al.* (2021) 'A simple method for quantitating confocal fluorescent images', *Biochemistry and Biophysics Reports*, 25. doi: 10.1016/j.bbrep.2021.100916.

Sodhi, R. K., Singh, N. and Jaggi, A. S. (2010) 'Poly(ADP-ribose) polymerase-1 (PARP-1) and its therapeutic implications', *Vascular Pharmacology*, pp. 77–87. doi: 10.1016/j.vph.2010.06.003.

Solomon, D. A. *et al.* (2011) 'Mutational Inactivation of STAG2 Causes Aneuploidy in Human Cancer', *Science*, 333(6045), pp. 1039–1043. doi: 10.1126/science.1203619.Mutational.

Solomon, D. A. *et al.* (2013) 'Frequent truncating mutations of STAG2 in bladder cancer', *Nature Genetics*, 45(12). doi: 10.1038/ng.2800.

Taylor, C. F. *et al.* (2014) 'Frequent inactivating mutations of STAG2 in bladder cancer are associated with low tumour grade and stage and inversely related to chromosomal copy number changes', *Human Molecular Genetics*, 23(8). doi: 10.1093/hmg/ddt589.

Thomas, S. E. *et al.* (2005) 'Identification of Two Proteins Required for Conjunction and Regular Segregation of Achiasmate Homologs in Drosophila Male Meiosis', *Cell*, 123(4), pp. 555–568. doi: 10.1016/j.cell.2005.08.043.

Thota, S. *et al.* (2014) 'Genetic alterations of the cohesin complex genes in myeloid malignancies.', *Blood*, 124(11). doi: 10.1182/blood-2014-04-567057.

Tirode, F. *et al.* (2014) 'Genomic landscape of ewing sarcoma defines an aggressive subtype with co-association of STAG2 and TP53 mutations', *Cancer Discovery*, 4(11). doi: 10.1158/2159-8290.CD-14-0622.

Wang, L. B. *et al.* (2021) 'Proteogenomic and metabolomic characterization of human glioblastoma', *Cancer Cell*, 39(4). doi: 10.1016/j.ccell.2021.01.006.

Weinstein, J. N. *et al.* (2014) 'Comprehensive molecular characterization of urothelial bladder carcinoma', *Nature*, 507(7492). doi: 10.1038/nature12965.

Wu, J. S. and Luo, L. (2006) 'A protocol for dissecting Drosophila melanogaster brains for live imaging or immunostaining', *Nature Protocols*, 1(4). doi: 10.1038/nprot.2006.336.

Zhao, J. *et al.* (2019) 'Immune and genomic correlates of response to anti-PD-1 immunotherapy in glioblastoma', *Nature Medicine*, 25(3). doi: 10.1038/s41591-019-0349-y.

Zhou, J. *et al.* (2023) 'STAG2 Regulates Homologous Recombination Repair and Sensitivity to ATM Inhibition', *Advanced Science*, 10(36). doi: 10.1002/advs.202302494.

Figures

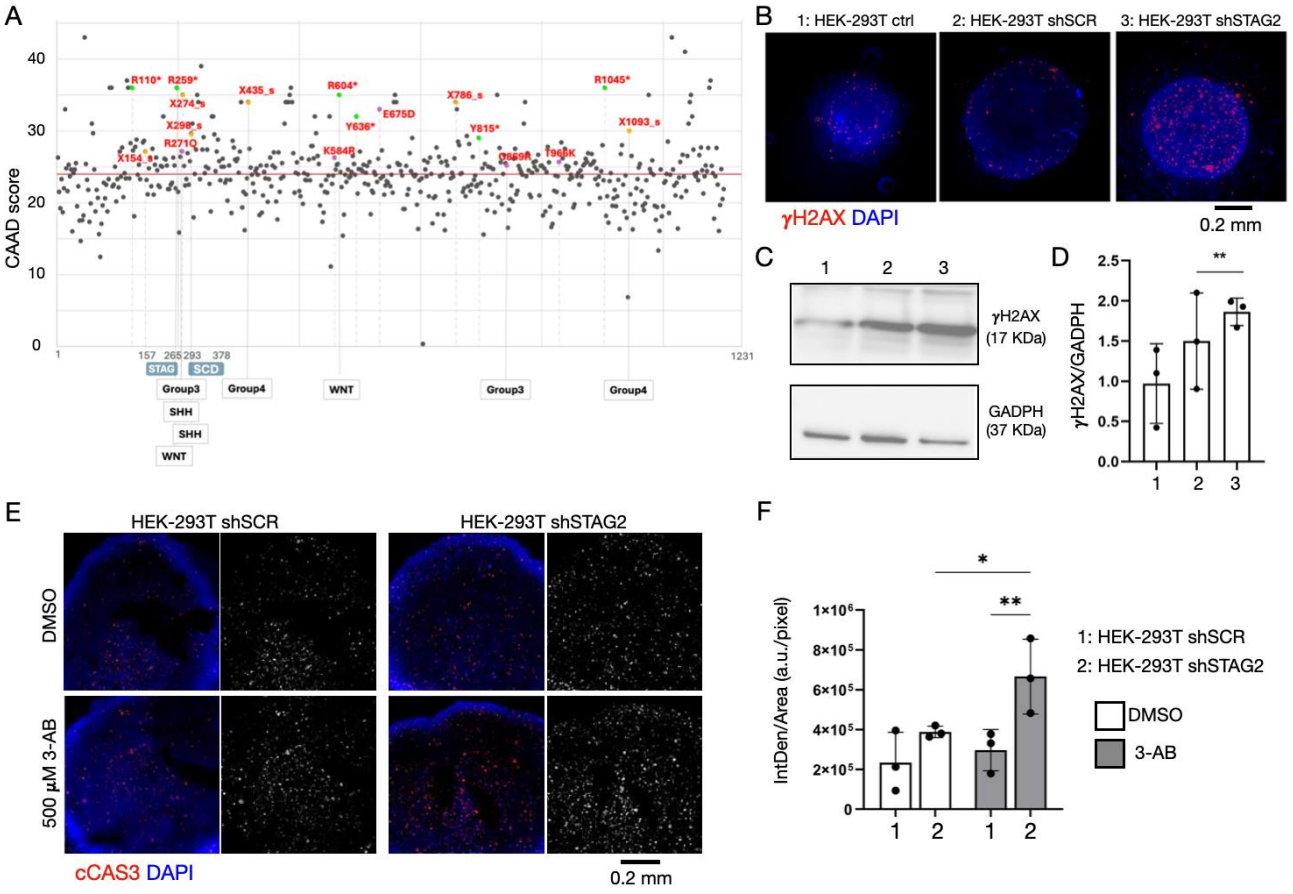

Fig. 1. STAG2 variants in brain cancer, *STAG2* depletion and PARP inhibitor treatment in human cells. (A) Variants in STAG2 observed in medulloblastoma and glioblastoma are deleterious. The graph displays the CADD value (y-axis), a score of variant deleteriousness, for all the STAG2 variants reported in the genome aggregation database gnomAD (grey) and in the cancer genomic database cBioPortal (in color). Missense variants associated with medulloblastoma and glioblastoma are shown as colored dots. Purple indicates missense, green nonsense and yellow splicing variants. 3 frameshift variants found in medulloblastoma and glioblastoma are not reported. Gray variants are mainly found in Mulleghama-Klein-Martinez syndrome patients. The amino acid position of the aa changes is shown on the x-axis and above the medulloblastoma and glioblastoma variants. The average CADD value of variants is indicated by the red line. Below the graph, labels indicate the molecular subtyping of medulloblastoma for the indicated variants. (B) Confocal sections of control HEK-293T spheroids or spheroids stably expressing a scrambled control shRNA (shSCR) or a shRNA targeting *STAG2* (shSTAG2) treated to label DNA (DAPI) and DNA damage foci (γH2AX). (C-D) Western blot analysis of the indicated extracts to detect γH2A.X and GADPH levels and relative quantification. In D, each data point represents a biological replicate. HEK-293T

shSTAG2 samples were compared to HEK-293T shSCR by one-way ANOVA, with uncorrected Dunnett's multiple comparison test. (E-F) Confocal sections of the indicated spheroids treated as indicated and labeled to detect the DNA (DAPI) and the apoptotic marker cleaved Caspase 3 (cCas3) and relative quantification. In F, each data point represents a biological replicate. The 3-AB shSTAG2 sample was compared to 3-AB shSCR or vehicle-treated shSCR by one-way ANOVA, with uncorrected Fisher's LSD test. All other comparisons are non-significant.

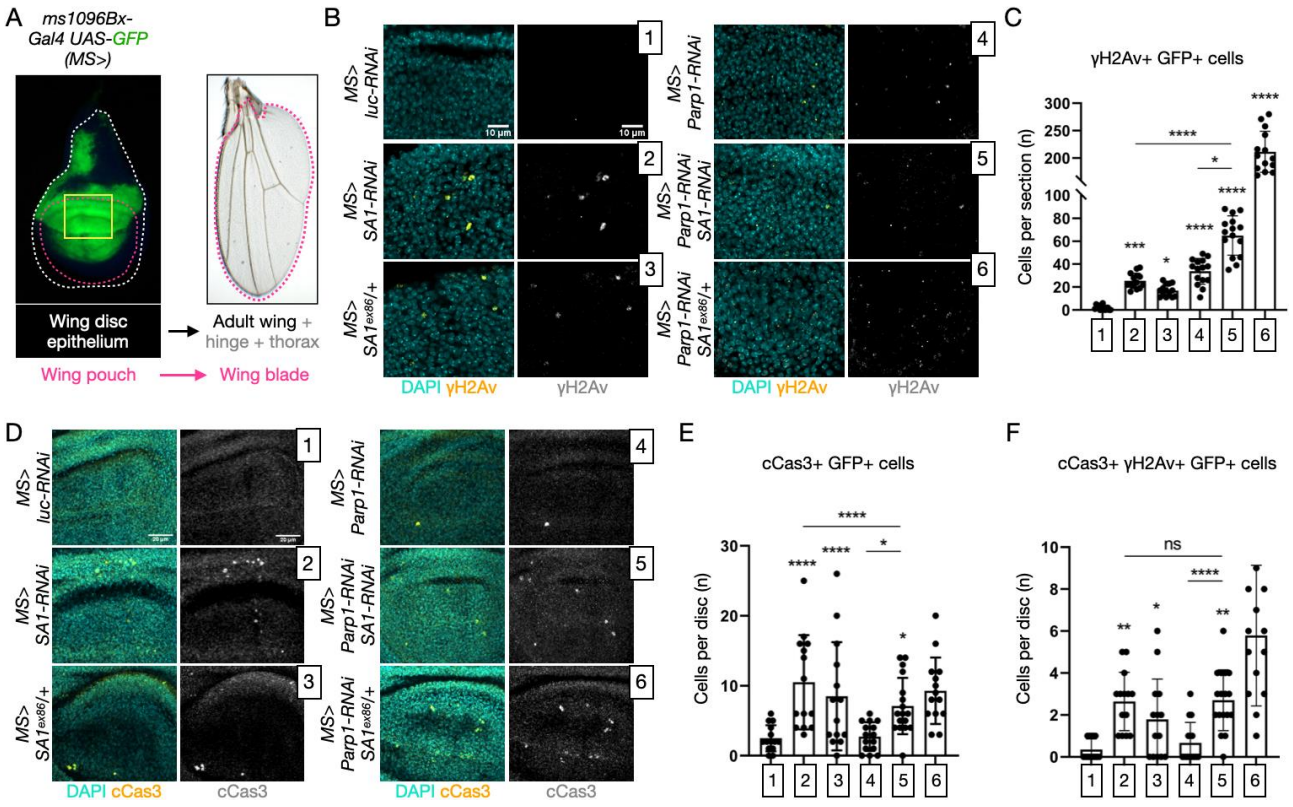

Fig. 2. DNA damage and apoptosis upon *in vivo* downmodulation of cohesin and PARP activity. (A) Schematics of wing imaginal discs illustrating their structure, fate and domain of misexpression using MS-Gal4 UAS-GFP (MS>GFP) to mark the tissue impacted by the depletions. The area analyzed in the experiment described in this figure is highlighted by the yellow box. (B-C) Single confocal sections of the GFP-positive dorsal portion of the wing pouch depleted as indicated and treated to label DNA (DAPI) and DNA damage foci (γH2Av) and relative quantification. Sections were analyzed to count the number of cells with γH2Av signal. Samples were compared by one-way ANOVA, with uncorrected Fisher's LSD. P-values intervals above the bars indicate comparisons with sample 1, while lines indicate other meaningful comparisons. Each data point in C represents a single disc section. N>14 sections analyzed. **(**D-F) Confocal sections of the pouch of imaginal discs depleted *in vivo* as indicated, treated to label cleaved Caspase 3 (cCas3) and relative quantification (E-F). Z-stacks of the GFP-positive portion of the wing discs were scored to count the average number of cells with cCas3 signal. Samples were compared by one-way ANOVA, with uncorrected Fisher's LSD. P-values intervals above the bars indicate comparisons with sample 1, while lines indicate other meaningful comparisons. Each data point in E-F represents a Z-stack. N>14 sections analyzed.

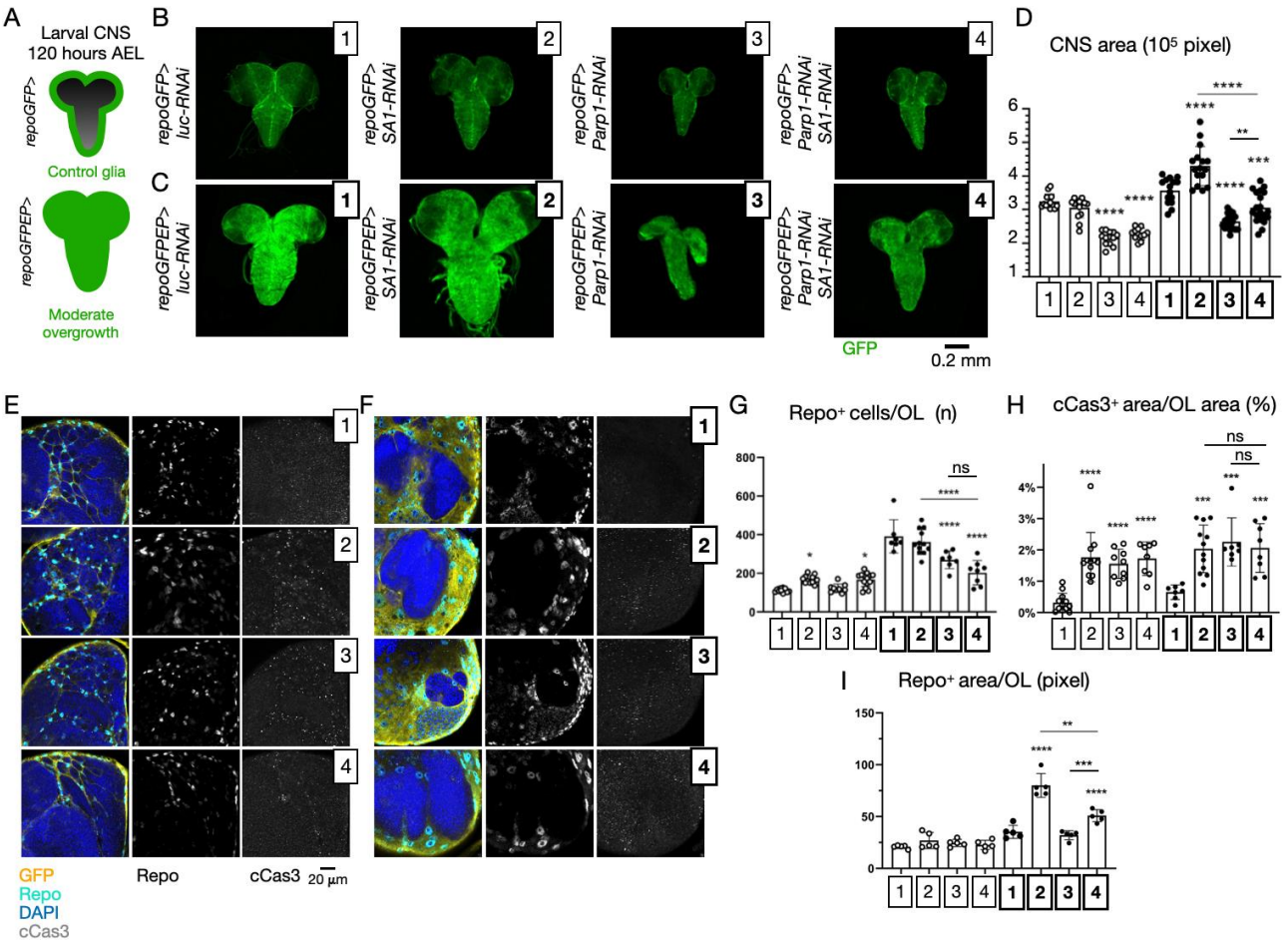

Fig. 3. Tumor suppressive activity of cohesin genes in an *in vivo* glioma model. (A) Schematics of the gliomagenesis model in *Drosophila* larvae. *repoGFPEP* larvae at 120 hours AEL display a moderate overgrowth that constitute a useful sensitized background to evaluate the effects of genetic modulations. (B-D) Maximum projection of confocal z-stack spanning the entire larval CNS of animals of the indicated genotype and relative quantification of the CNS area (D). The area of >14 CNS per sample is indicated. Samples were compared by one-way ANOVA, with Šídák's multiple comparisons test. P-values intervals above the bars indicate comparisons with sample 1, while lines indicate other meaningful comparisons. (E-I) Single medial section of the CNS labelled as indicated and associated quantifications (G-I). Genotypes are as in panel B-C. In G-H, each data point represents the number of Repo+ cell per optic lobe (G), or the percentage of the cCas3+ signal over the optic lobe area. N>7 optic lobes per sample were analyzed. In I, each data point represents the mean area of 20 cells. n=5 optic lobes per sample. Samples in G-I were compared by one-way ANOVA, with Šídák's multiple comparisons test. P-values intervals above the bars indicate comparisons with sample 1, while lines indicate other meaningful comparisons.

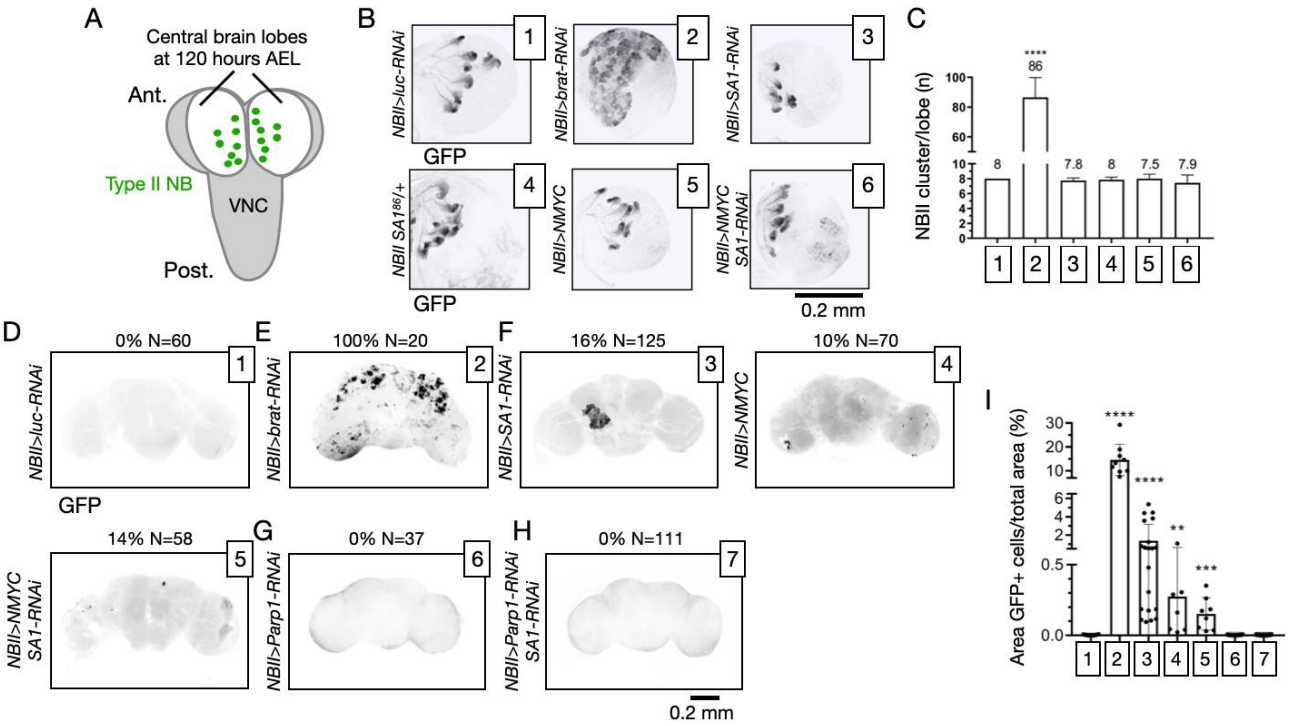

Fig. 4. Formation of masses upon manipulation of oncogenes and *SA1* expression in neural stem cells. (A) Schematics of NB positioning in the larval CNS at 120 AEL. (B-C) Maximum projection of confocal z-stack spanning optic lobes of the indicated genotypes showing GFP expression associated to NBII. Quantification of NBII number per optic lobe upon modulation of the indicated genes (C) N>6 optic lobes per sample. Samples were compared by one-way ANOVA, with Šídák's multiple comparisons test. P-values intervals above the bars indicate comparisons with sample 1. **(**D-G) Maximum projection of confocal z-stack spanning adult brains of the indicated genotypes showing GFP signal or lack of thereof. (I) Quantification of the area of the brain covered by GFP+ masses. Samples as in D-G. Each data point represents one brain positive for GFP. N>7 brains analyzed. Samples were compared by uncorrected Kruskal–Wallis test. P-values intervals above the bars indicate comparisons with sample 1.

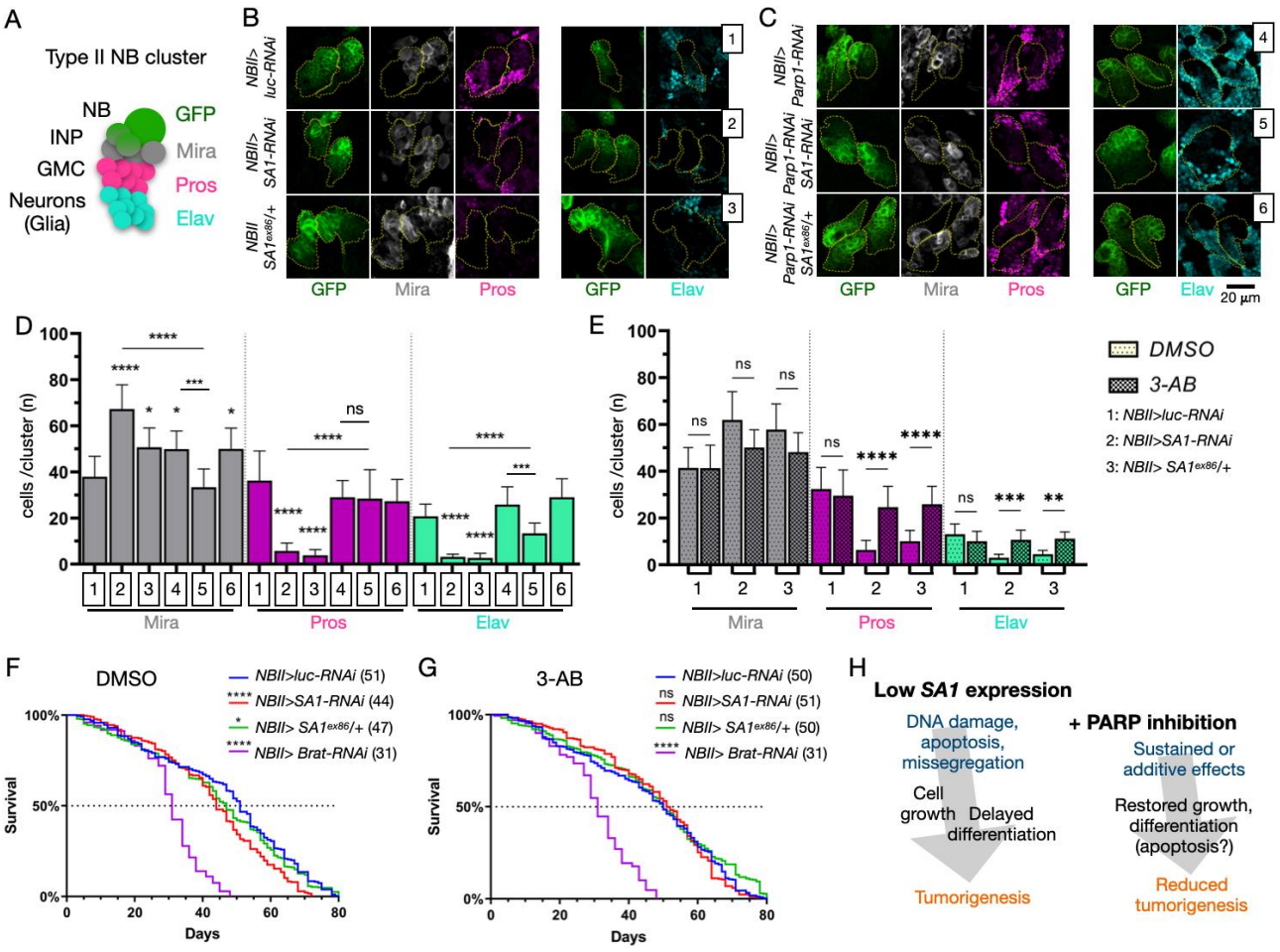

Fig. 5. Developmental and lifespan alteration upon *SA1* depletion in developing neuroblasts are rescued by reduction of PARP activity. (A) Schematics of NBII development and relative markers used to assess it. **(**B-C) Representative confocal images of NBII clusters of the indicated genotypes, labeled to detect the indicated differentiation markers. **(**D-E) Quantification of the indicated differentiation marker in NBII cluster of the indicated genotype (D), or upon supplementation with vehicle (DMSO) alone or 2.5 µM 3-AB in vehicle (3-AB) (E). More than 4 brain lobes per sample were analyzed, representing a minimum of 22 NBII cluster, were used for the quantification. Samples were compared by one-way ANOVA, with uncorrected Dunn's multiple comparison test. P-values intervals above the bars indicate comparisons with sample 1, while lines indicate other meaningful comparisons (D), P-values intervals above the bars indicate comparisons between treated and untreated samples (E). (F-G) Lifespan of animals of the indicated genotype fed with vehicle alone (DMSO) or 2.5 µM 3-AB in vehicle. Numbers in brackets indicate the day at which the population has reached 50% survival. The experiment was repeated twice with n>250 animals per sample. Data of both experiments have been pooled and are shown as a single survival curve. Samples were pairwise compared with *NBII>luc-RNAi* controls using a Log-rank (Mantel-Cox) test. P-values intervals in the legend indicate comparisons with *NBII>luc-RNAi*. (H) A model of tumorigenesis based on reduced *SA1* expression and effects of PARP inhibition in such context.

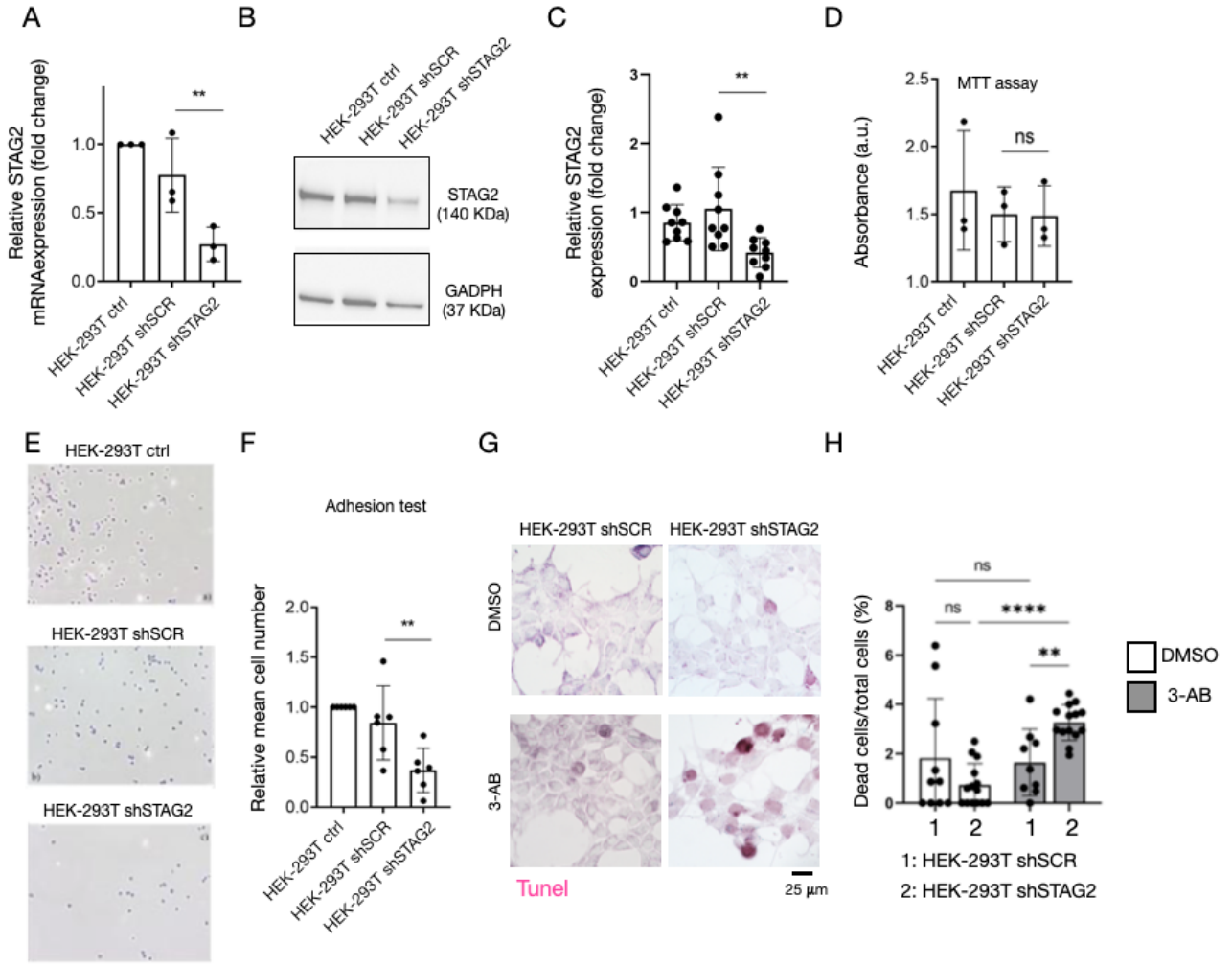

Fig. S1. *STAG2* depletion affects cell adhesion. (A) RT-PCR quantification of *STAG2* mRNA expression in control cells or cells expressing the indicated shRNA. Each data point represents a biological replicate. shSTAG2 and shSCR samples were compared by one-way ANOVA, with uncorrected Fisher's LSD test. (B-C) Western blot analysis of STAG2 and GADPH expression in control cells or cells expressing the indicated hairpin. The blot of GADPH to normalize is the same of Fig. 1C. Each data point represents a technical replicate across 3 biological replicates. shSTAG2 and shSCR samples were compared by one-way ANOVA, with uncorrected Dunnett's multiple comparison test. (D) Determination of cell density of control cells or cells expressing the indicated hairpin. Each data point represents a technical replicate. shSTAG2 and shSCR samples were compared by one-way ANOVA, with uncorrected Fisher's LSD test. (E-F) Substrate adhesion of control cells or cells expressing the indicated shRNA and relative quantification. shSTAG2 and shSCR samples were compared by one-way ANOVA, with uncorrected Fisher's LSD test. (G-H) Representative brightfield

images of the indicated HEK-293T cell lines treated with DMSO or 3-AB at a concentration of 500uM, and relative quantification (H). The percentage of TUNEL+ cells per sample is illustrated. Each data point represents a technical replicate across 3 biological replicates. the The 3-AB HEK-293T shSTAG2 sample was compared to HEK-293T shSTAG2 treated with DMSO or to HEK-293T shSTAG2 shSCR treated with 3-AB by one-way ANOVA, with uncorrected Fisher's LSD test.

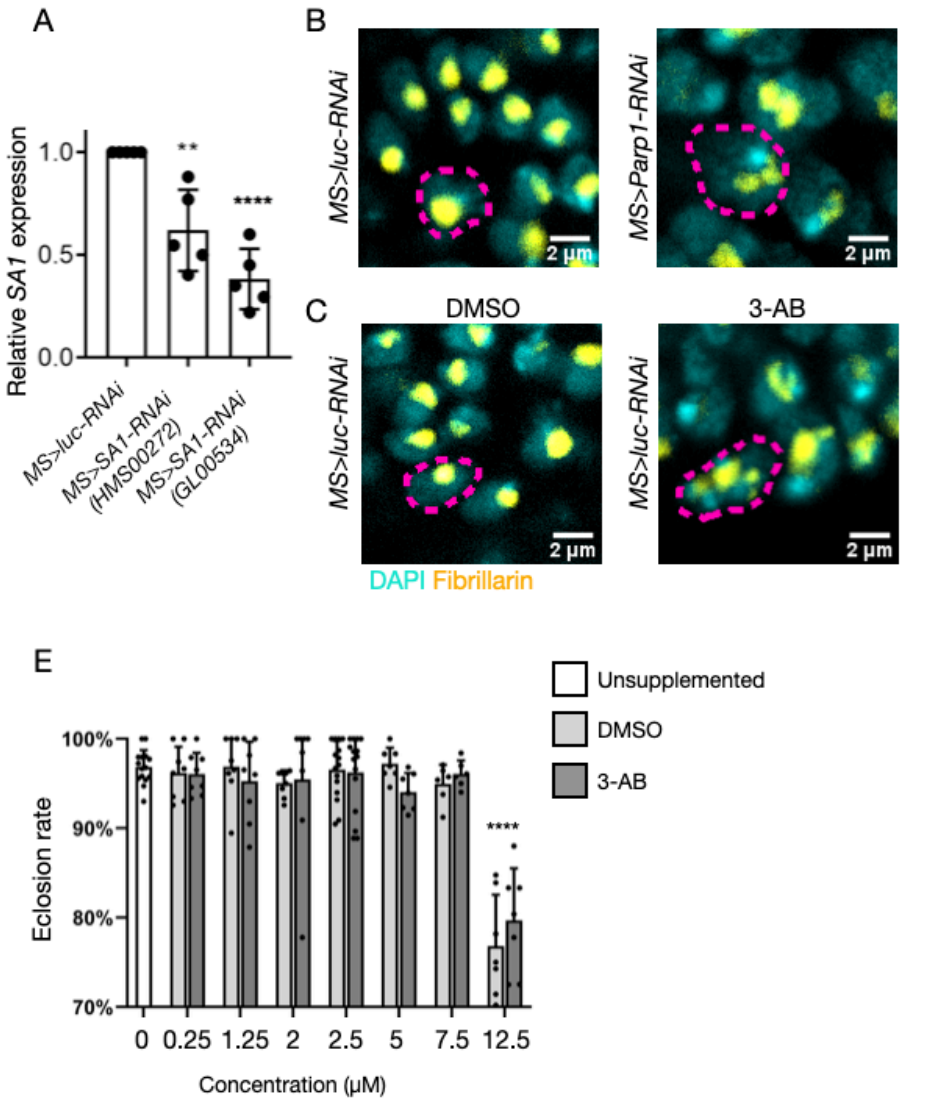

Fig. S2. *SA1* downregulation and reduction of PARP activity. (A) RT-PCR quantification of *SA1* mRNA expression in extracts of wing imaginal discs of the indicated genotypes. Each data point represents extracts of 30 wing discs. Samples were compared to *MS>luc-RNAi* controls by one-way ANOVA, with uncorrected Fisher's LSD. (B-C) High magnification single section confocal images of nuclei of the wing pouch of animals of the indicated genotypes treated with vehicle (DMSO) or 2.5 µM 3-AB in vehicle (3-AB), that have been labeled to detect the DNA (DAPI) and the nucleolar marker fibrillarin. Example nuclei are enclosed by dashed lines. (D) Quantification of nucleolar fragmentation. Each data point represents a single disc in which 20 nuclei scored for fragmentation. N=5 discs. Samples were compared to controls by unpaired t-test. (E) Eclosion rates of control animals untreated or fed with the indicated concentration of vehicle alone (DMSO) or 3-AB in vehicle (3-AB). Each data point represents 1 fly vial. N>7 vials analyzed. Mock-treated and treated samples were compared by two-way ANOVA, with uncorrected Fisher's LSD.

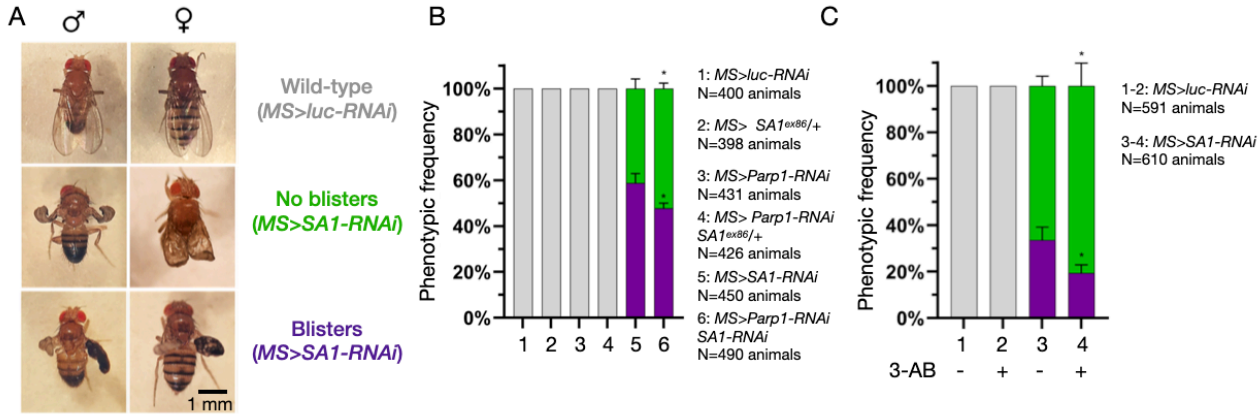

Fig. S3. Amelioration of *SA1* depletion phenotypes upon reduction of PARP activity. (A) Classification of wing phenotypes of control animals or animals with *SA1* downmodulation. (B-C) Quantification of the wing phenotypes of animals of the indicated genotypes and treated as indicated. In C, 3-AB was used at 2.5 µM in the food. The number of analyzed animals of each condition is >400. Samples were compared by two-way ANOVA, with Šídák's multiple comparisons test. P- values intervals above the bars indicate comparisons with sample 5 (B) or 3 (C).

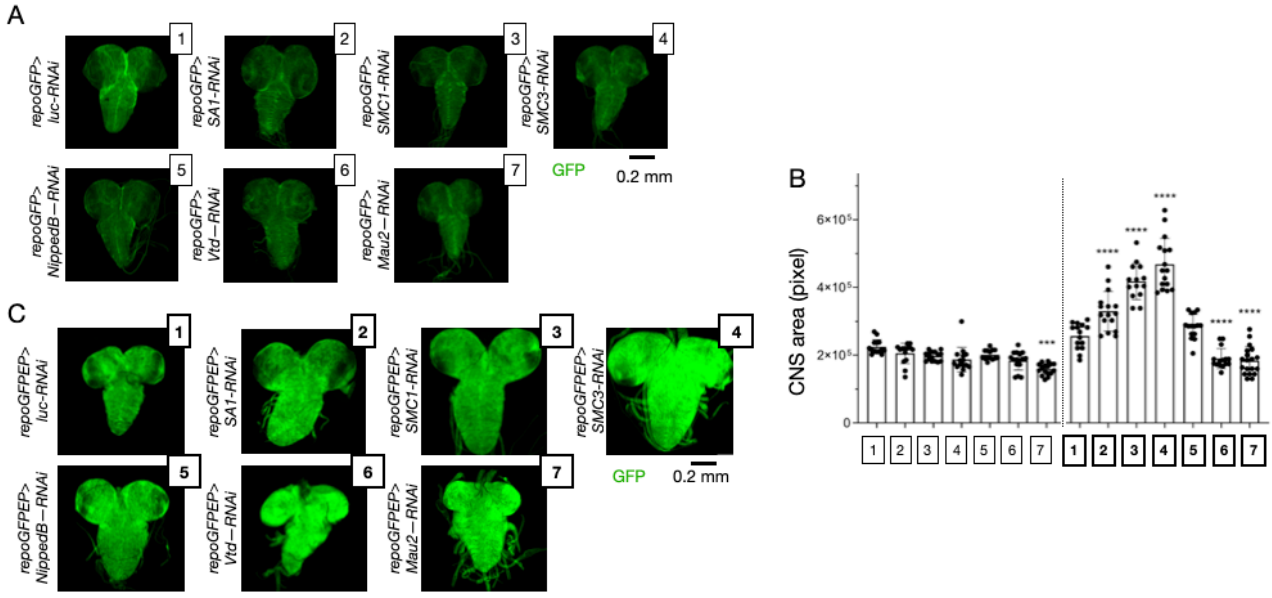

Fig. S4. Cohesin complex depletion during gliomagenesis. (A-C) Maximum projection of confocal z-stack spanning the entire larval CNS of animals of the indicated genotype (A, C) and relative quantification (B). In B, the area of >12 CNS per sample is indicated. In both graphs, samples were all compared to control (sample 1) by one-way ANOVA, with Šídák's multiple comparisons test.

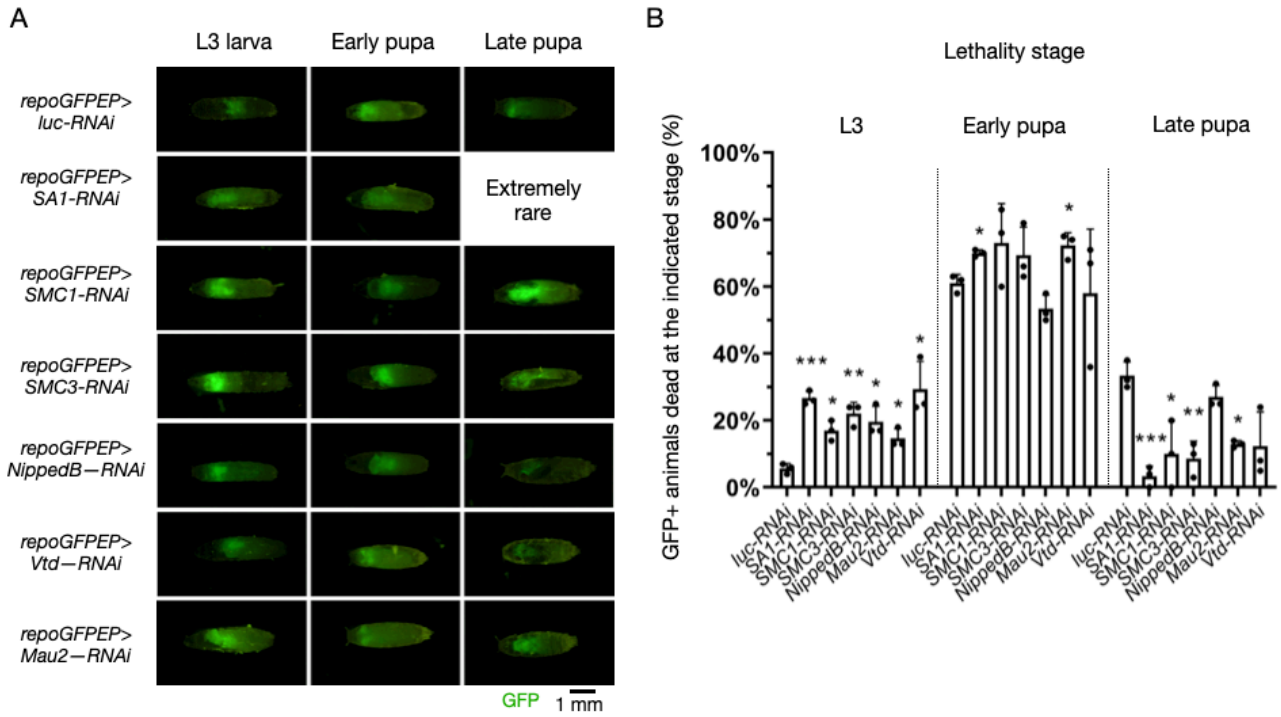

Fig. S5. Lethality stage of animals with reduced cohesin gene expression. (A-B) Representative fluorescence images of *repo>GFPEP* larvae depleted of the indicated cohesin gene and quantification of their lethality stage. The average of 3 experiments is presented with>30 animals per sample. Samples were compared to luc-RNAi controls by two-way ANOVA, with uncorrected Fisher's LSD.

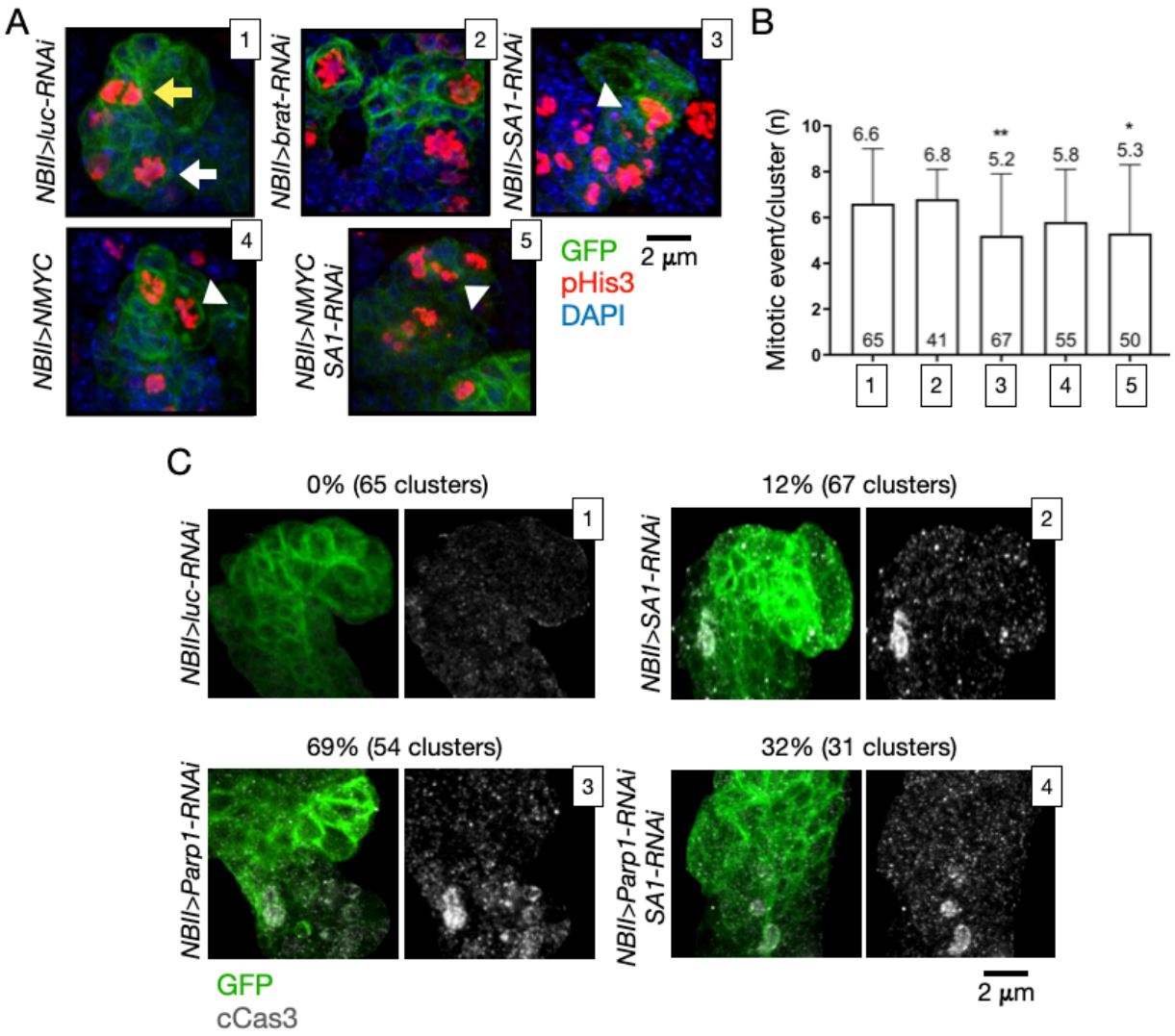

Fig. S6. Profiling of NBII clusters. (A-B) Representative single section confocal images of NBII clusters of the indicated genotypes, labeled to detect the cell proliferation marker pHis3 and relative quantification (B). In A, the yellow and white arrow point to a normal anaphase and prophase, respectively, while the arrowhead points to examples of aberrant mitotic features. In B, the number of clusters analyzed for each sample is listed at the base of each bar. Samples were all compared to control (sample 1) by one-way ANOVA, Dunnett's multiple comparisons test. (C) Representative maximal projections of a z-stack of confocal section of NBII clusters of the indicated genotypes, labeled to detect the apoptosis marker cCas3 and relative quantification of the frequency of cCas3+ cells and number of clusters analyzed. Please note that the average number of cCas3+ cells in the clusters that are found cCas3+ is of 1 in sample 2, 2.7 in sample 3 and 1.4 in sample 4.

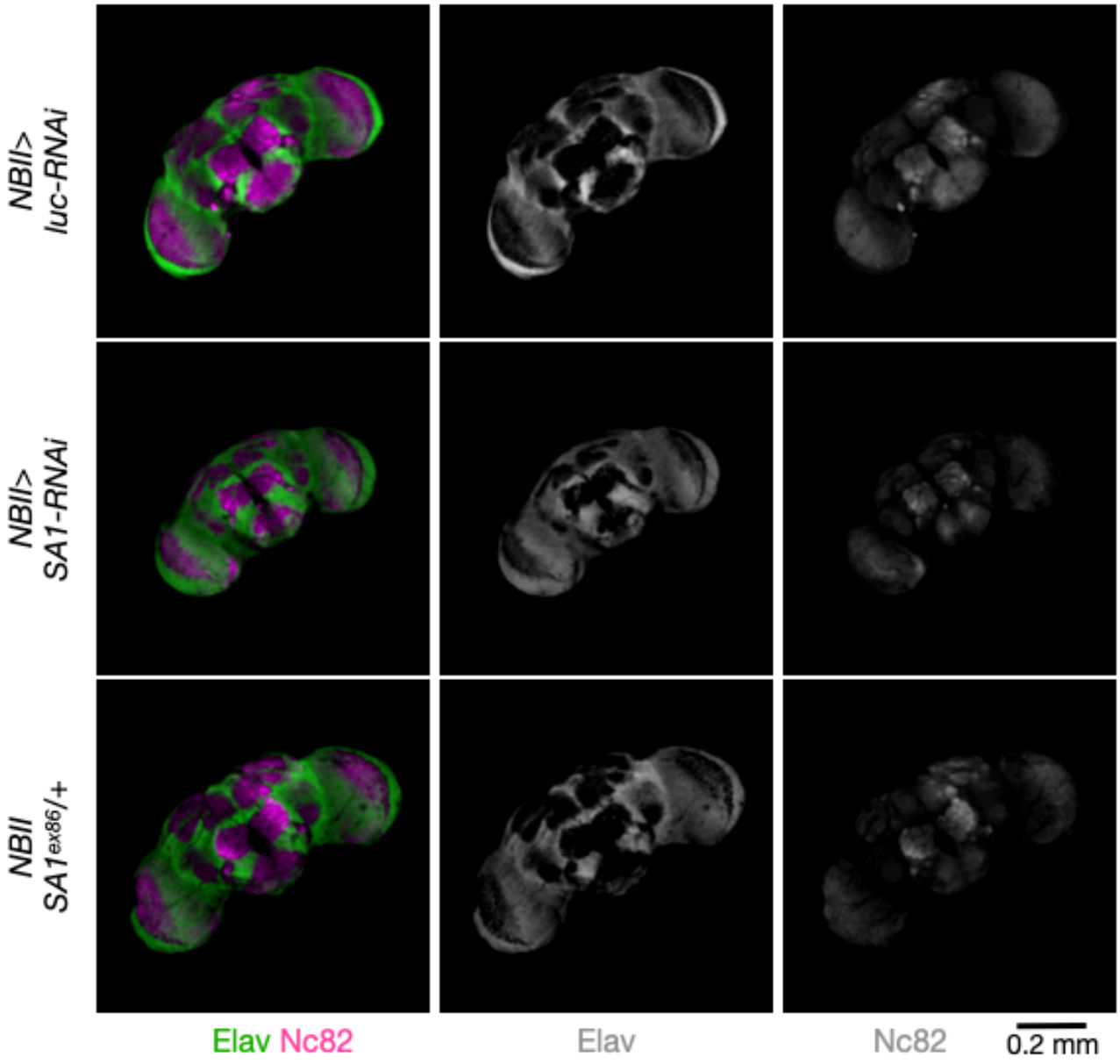

Fig. S7. Brain morphology with differing levels of SA1 expression. Confocal images of dissected adult brains of the indicated genotype, immunolabeled to detect the indicated protein markers. Nc82 marks the neuropils, while Elav marks the nucleus of neurons allowing to discriminate the adult brain morphology.

Table S1.

Available for download at
https://journals.biologists.com/dmm/article-lookup/doi/10.1242/dmm.052440#supplementary-data